



Effects of cloud microphysics on the simulation of extreme precipitation over the Tibetan Plateau region

Irene Elisa Bellagente ^{a,b}, Hui-Wen Lai ^{a,*}, Fabian Senf ^b

^a Department of Earth Sciences, University of Gothenburg, Gothenburg, Sweden

^b Department of Modelling of Atmospheric Processes, Leibniz Institute for Tropospheric Research, Leipzig, Germany

ARTICLE INFO

Keywords:

Precipitation
WRF
Convection-permitting simulations
Cloud microphysics scheme
Tibetan Plateau

ABSTRACT

Extreme precipitation plays a critical role in the development of hydrological extremes with severe socio-economic and environmental impacts. Over the Tibetan Plateau (TP), extreme precipitation events have increased in frequency and intensity and are projected to rise further under climate change. However, simulations of such events in this region remain challenging due to uncertainties in the representation of cloud microphysics. While previous research has exposed the sensitivity of climate models to microphysics schemes, the atmospheric processes driving discrepancies in precipitation simulations are still not fully explored. In this study, we analyse two extreme precipitation events over the TP region using six different microphysics schemes in the Weather Research and Forecasting model (WRF). We assess how precipitation and related processes are represented across these schemes and identify key sources of uncertainties in precipitation simulations. Our findings reveal substantial variations in the location, intensity and timing of precipitation, with differences in accumulated amounts reaching up to 40 % depending on the microphysics scheme used. Further analysis shows that the timing and strength of convective activity are closely linked to precipitation patterns, leading to significant discrepancies across experiments. Additionally, the representation of horizontal water vapour transport plays a critical role in determining the location and intensity of precipitation by influencing moisture availability. Lastly, the modelling of cloud composition – particularly of solid-phase hydrometeors – emerges as a crucial factor in precipitation evolution, contributing substantially to the variability in simulated precipitation location and intensity.

1. Introduction

Extreme precipitation plays a critical role in the development of hydrological extremes with severe socio-economic and environmental impacts such as floods and landslides. Over the Tibetan Plateau (TP), extreme precipitation events have increased in frequency and intensity in recent decades and are projected to rise further under climate change (Karki et al., 2017; Pörtner et al., 2019). Since the TP region serves as a crucial water source for nearly two billion people through its major river systems (Douville et al., 2021; Immerzeel et al., 2020), understanding the mechanisms driving extreme precipitation is essential for effective water resource management and disaster risk reduction. However, substantial uncertainties remain in simulating such events due to the complex topography of the plateau and the intricate interplay between atmospheric dynamics, thermodynamics, and cloud microphysics (Prein et al., 2023). Reducing these uncertainties is important for improving

both weather predictions and climate projections in this vulnerable region.

Extreme precipitation can occur throughout the year over the TP region, producing daily totals of about 10–30 mm depending on seasons and locations (Ayantobo et al., 2022). Average annual precipitation varies widely across the plateau, with the northeast receiving around 100 mm and the southwest up to 800 mm (Xu et al., 2008). Extreme precipitation is often driven by interactions between the dominant atmospheric processes over the TP region, including large-scale monsoonal circulations, surface heating, moisture transport and orographic forcing (Lai et al., 2024; Maussion et al., 2014). These interactions contribute through the formation of mesoscale convective systems (MCSs), Tibetan Plateau vortices (TPVs), and lake-effect snow (Kukulies et al., 2023a; Lin et al., 2022; Lin et al., 2023). Changes in extreme precipitation patterns have already intensified hydrological extremes in recent decades, increasing flood risks in the northeastern TP

* Corresponding author.

E-mail address: hui-wen.lai@gu.se (H.-W. Lai).

and worsening drought conditions in the southeast (Bao et al., 2024; Shao et al., 2023). These trends highlight the need to understand the mechanisms driving extreme precipitation events and how they are represented in numerical models to more accurately anticipate future changes.

Numerical weather prediction (NWP) models are valuable and commonly used tools in weather and climate studies. Global climate models (GCMs), despite their ability to capture large-scale weather and climate patterns, struggle to accurately represent local processes due to their coarse spatial and temporal resolution (Gao et al., 2018; Lin et al., 2018; Orr et al., 2017). Simulations in the Coupled Model Intercomparison Project phase 6 (CMIP6) have been shown to still retain biases from previous versions and overestimate precipitation over the TP (Lin et al., 2021). Moreover, models with parameterised convection largely fail to reproduce major precipitation events, such as mesoscale convective systems (MCSs) (Feng et al., 2018). Regional climate models (RCMs) can simulate climate at much finer spatial scales, offering better representation of interactions between large-scale circulations and regional precipitation mechanisms such as orographic lifting (Orr et al., 2017). The Weather Research and Forecasting (WRF) model is one of the most widely adopted and state-of-the-art mesoscale NWP models. Over the Himalayas, high-resolution WRF simulations have shown improved spatial and temporal variations of simulated precipitation due to a more detailed representation of terrain, land use, and the explicit treatment of convection (Karki et al., 2018). In fact, recent advancements in computational resources have enabled RCM simulations to be run at convection-permitting resolutions (≤ 4 km grid spacing), eliminating the need for parameterizations (Podeti et al., 2020; Prein et al., 2023). Convection-permitting models (CPMs) produce more realistic timing and intensity of summertime precipitation and better reproduce high intensity precipitation events (Feng et al., 2018; Kukulies et al., 2023b).

In climate models, cloud microphysics is parametrised using micro-physics schemes that simulate the formation, growth and fallout of various hydrometeors. Previous research has revealed that microphysics schemes have a greater impact on summer precipitation over the TP region than other parameterization schemes, such as those for radiation and planetary boundary layer (Lv et al., 2020; Orr et al., 2017). Differences in the formulation of microphysics schemes have been found to play a vital role in simulating the thermodynamic profile that influences the intensity of convection responsible for heavy rainfall (Karki et al., 2018; Thomas et al., 2021). Other studies have highlighted that liquid- and ice-phase microphysics in microphysics schemes play a critical role in the simulation of cloud dynamics and thermodynamics processes as well as precipitation intensity over the TP (Hazra et al., 2020; Tang et al., 2019). A study that performed ensemble-physics experiments over the TP also suggests that microphysics schemes are one of the leading sources of uncertainties in the modelling of precipitation (Prein et al., 2023).

While the consequences of using different microphysics schemes have been pointed out, the atmospheric processes and main factors contributing to precipitation differences among the schemes are not fully explored. A recent study focusing on the summer of 2018 conducted sensitivity tests on precipitation response to microphysical parameterizations in WRF (Zhou et al., 2024), providing valuable information on the role of the spatial distribution of horizontal water vapour transport and the vertical profiles of hydrometeors. However, knowledge gaps remain, particularly regarding how microphysical processes influence precipitation under different seasonal conditions that lead to heavy precipitation events. Our work provides new insights by investigating two precipitation events - one in summer and one in autumn – at convection-permitting scales, offering a broader perspective on microphysical processes under varying atmospheric conditions. We examine the effects of convective activity, moisture transport and cloud phase on precipitation formation, further advancing our understanding of how microphysical uncertainties influence simulated precipitation. We address three research questions:

1. Assess the spatial and temporal differences of precipitation using WRF simulations at convection-permitting scale with various microphysics schemes and evaluate them against observation and reanalysis datasets.
2. Investigate the simulated atmospheric processes by studying the atmospheric instability, moisture transport and hydrometeors distributions.
3. Identify the key factors leading to uncertainties in precipitation simulations with different microphysics schemes.

This study examines atmospheric instability through the analysis of equivalent potential temperature and convective available potential energy; investigates the moisture transport by evaluating both the vertically integrated water vapour transport and vertical moisture flux; and assesses the role of cloud composition by analysing liquid and ice water paths, along with the vertical distribution of individual hydrometeors. The results contribute to a better understanding of the sensitivity of extreme precipitation to microphysical processes, and lay the groundwork for future improvements of microphysics parametrisations in WRF to provide more accurate and consistent simulations of extreme precipitation events over the TP region.

2. Data and methods

2.1. Case studies

We selected two cases of extreme precipitation that are identified by the CORDEX (Coordinated Regional Climate Downscaling Experiment) Flagship Pilot Study CPTP (Convection-Permitting Third Pole, http://rcg.gvc.gu.se/cordex_fps_cptp/). One case is associated with precipitation resulting from a MCS in July 2008, while the other event is related to a heavy snow system in October 2018.

2.1.1. Mesoscale convective system (MCS) – July 2008

On July 18, 2008, a Tibetan Plateau Vortex (TPV) developed in the western TP and moved eastward. It continued its trajectory towards the northeast until the Yellow Sea coast (Curio et al., 2019; Feng et al., 2014). Upon reaching the eastern TP, the TPV triggered a MCS, resulting in significant convective precipitation over the Yangtze River Basin (Fig. 1) (Kukulies et al., 2021). During this event, a weather station in the Sichuan Basin recorded a peak 24-h accumulated rainfall of 288 mm.

2.1.2. Heavy snow system (snow) – October 2018

In autumn 2018, a major snowfall event occurred over the southeastern TP, ranking among the most substantial snowfalls recorded at the Nam Co station since observations began in 2005 (Dai et al., 2020). On October 3, a cold air mass swept across the group lakes area around Nam Co, causing the region's daily minimum temperature to drop by approximately 4.5°C within 24 h. Snow accumulation during this event varied significantly, with areas east of Nam Co receiving over 50 cm, whereas the western region recorded only 5 cm (Fig. 1) (Dai et al., 2020).

2.2. Datasets

2.2.1. Validation datasets

Several observations, including both satellite- and ground-based, and a global reanalysis dataset were used for modelling evaluation and comparison (Table 1). The used datasets are NASA's Global Precipitation Measurement Integrated Multi-satellE Retrievals (IMERG), Global Land Data Assimilation System (GLDAS), Asian Precipitation-Highly Resolved Observational Data Integration Towards Evaluation of Water Resources (APHRODITE), Multi-Source Weighted-Ensemble Precipitation (MSWEP) and ERA5 reanalysis data provided by the European Centre for Medium-Range Weather Forecast (ECMWF) (Beck et al., 2019; Hersbach et al., 2020; Huffman et al., 2020; Rodell et al., 2004;

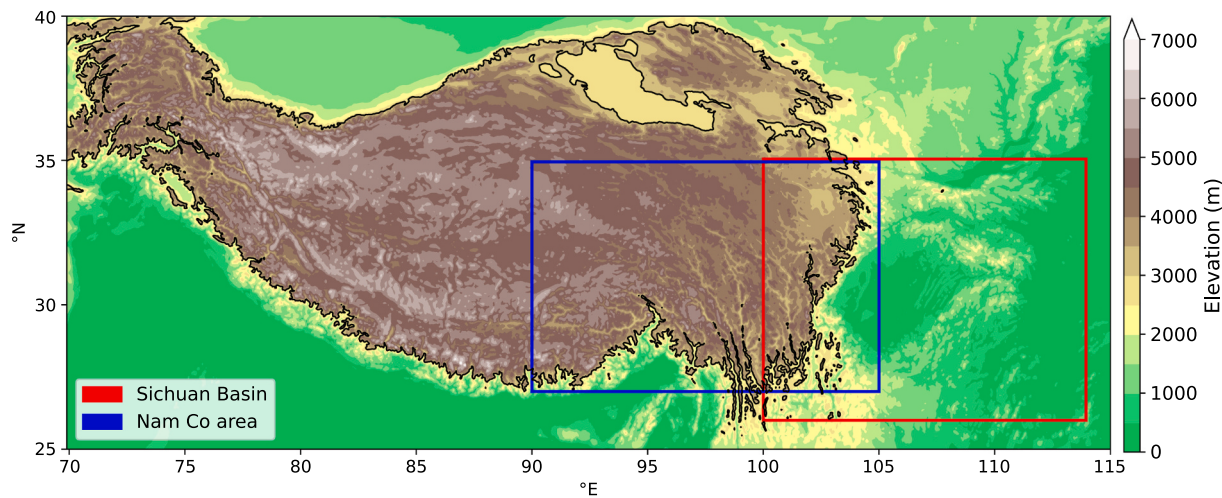


Fig. 1. WRF model domain D1 for the convection-permitting modelling over the Tibetan Plateau and surrounding areas. The red domain identifies the study region for the MCS case in Sichuan Basin, and the blue domain identifies the study region for the snow case around Nam Co area. Colour shading indicates the elevation. The black contours indicate elevation at 3000 m. (For interpretation of the references to colour in this figure legend, the reader is referred to the web version of this article.)

Table 1
Overview of validation datasets.

Name	Type	Horizontal resolution	Temporal resolution
IMERG	Satellite	$0.1^\circ \times 0.1^\circ$	Half-hourly
GLDAS	Satellite and ground	$0.25^\circ \times 0.25^\circ$	Three-hourly
APHRODITE	Rain-gauge	$0.25^\circ \times 0.25^\circ$	Daily
MSWEP	Satellite, ground and reanalysis	$0.1^\circ \times 0.1^\circ$	Three-hourly
ERA5	ECMWF reanalysis	$0.25^\circ \times 0.25^\circ$	Hourly

(Yatagai et al., 2012). For the MCS case we conducted the analysis on the area delimited by 26–35°N and 100–114°E from July 16, 2008, 00 UTC to July 24, 2008, 23 UTC, while for the snow case study the domain was delimited by 27–35°N and 90–105°E from October 4, 2018, 00 UTC to October 9, 2018, 23 UTC.

IMERG combines various satellite-based measurements to provide global precipitation products. It ensures quality control by prioritizing higher-quality microwave and radar/radiometer data, calibrating all inputs to a chosen high-quality standard, supplementing with lower-quality infrared data, and applying rain gauge data to correct biases (Pan et al., 2023). We used the half-hourly precipitation data from Level 3 product in version V06B with a spatial resolution of $0.1^\circ \times 0.1^\circ$. Previous studies over the TP have shown that IMERG performs relatively well in detecting precipitation compared to other satellite and model-based products (Kumar et al., 2021; Lyu et al., 2024).

GLDAS integrates ground and satellite precipitation data through an innovative software that includes both modelling and assimilation techniques. In GLDAS, precipitation quality control depends largely on the source data, with minimal internal correction, meaning accuracy varies depending on the quality and bias correction applied to the selected forcing dataset (Wang et al., 2021). It provides three-hourly variables products with a horizontal resolution of $0.25^\circ \times 0.25^\circ$. The precipitation rates were retrieved from version V2.1 and used for precipitation assessment. Previous studies over the TP suggest that GLDAS performs relatively well in simulating precipitation, especially snowfall, compared to other precipitation products and using gauge observations as reference (Ding et al., 2024; Yuan et al., 2021).

APHRODITE provides precipitation products based on rain gauge data across Asia, available until 2015, with a $0.25^\circ \times 0.25^\circ$ spatial resolution. Its performance is largely dependent on the number and quality of provided rain gauges, as no adjustments or homogenization

are implemented (Tan et al., 2025). The daily precipitation from version APHRO_MA V1801R1 in APHRODITE was applied for precipitation evaluations. APHRODITE has been shown to outperform over other datasets in capturing precipitation amounts (Tan et al., 2020) and is often used as a “ground truth” reference for precipitation evaluation researches (e.g. Chen et al., 2018; Sohn et al., 2012). We only employed the APHRODITE products in the MCS case because the data is not available for the snow case in 2018.

MSWEP is a precipitation product merging gauge, satellite, and reanalysis data. It applies rigorous quality control by correcting for biases through gauge-based adjustment, and using quality screening to exclude unreliable inputs (Beck et al., 2017a). It has a $0.1^\circ \times 0.1^\circ$ horizontal resolution and it is available from 1979 to present. As part of the precipitation analysis, we used the three-hourly precipitation data from version V2.8. Overall MSWEP showed reliable performance around the globe in comparison to other precipitation datasets (Beck et al., 2017b; Deng et al., 2024).

ERA5 is the fifth generation of atmospheric reanalysis for climate data provided by the ECMWF, available for the whole globe from 1940 (Hersbach et al., 2020). Hourly estimates with a horizontal grid spacing of $0.25^\circ \times 0.25^\circ$ were employed in the study. Single-level variables, namely hourly mean total precipitation rate (hereafter precipitation rate) and convective available potential energy (CAPE), were used to assess the performance of WRF simulations in reproducing convective activity and associated precipitation. Additionally, variables on pressure levels have been used to determine equivalent potential temperature (θ_e), vertically integrated water vapour transport (IVT) and liquid/ice water path (LWP/IWP). They were derived using air temperature, specific humidity, u- and v-component of winds, specific cloud liquid/ice water content (qcloud/qice) and specific rain/snow water content (qrain/qsnow). ERA5 not always accurately reproduces precipitation amounts and timings but performs well in most temporal variabilities and spatiotemporal patterns of precipitation over the TP (Dai, 2024; Hu and Yuan, 2021; Wu et al., 2023).

We used IMERG as reference for precipitation analysis and ERA5 for convective activity, moisture transport and cloud composition. This choice has been based on the fact that they merge large amounts of data from different sources (satellite-, ground- and model-based), their high spatiotemporal resolution and the data availability for both case studies.

2.2.2. WRF simulations

The simulations were produced by the Advanced Research Weather

Research and Forecasting model (WRF) version 4.2. WRF is a state-of-the-art mesoscale numerical weather prediction system widely used for modelling across weather and climate time scales (Powers et al., 2017; Skamarock et al., 2019). The simulations were run at 4 km grid spacing over the whole TP region (Domain D1: delimited by 25–40°N and 70–115°E; Fig. 1). To assess the impact of different microphysical processes as represented in various microphysics schemes, we followed Prein et al. (2023) and conducted simulations using all six microphysics schemes available: Morrison 2-moment (hereafter Morrison; Morrison et al., 2009), Thompson (Thompson et al., 2008), CAM 5.1 5-class (hereafter CAM; Eaton, 2011), SBU-YLin (hereafter Ylin; Lin and Colle, 2011), WRF Double Moment 6-class (hereafter WDM6; Lim and Hong, 2010) and WRF Double Moment 7-class (hereafter WDM7; Bae et al., 2019). Several studies over the TP region on extreme summer precipitation indicate that Thompson and Morrison simulate the precipitation field more accurately, whereas WDM6 tends to perform poorly in comparison (Karki et al., 2018; Lv et al., 2020; Orr et al., 2017; Zhou et al., 2024). These findings are consistent with those of Prein et al. (2023), which suggest that WDM6 and WDM7 result in lower-than-average performances over the TP, while the other microphysical parametrisations – Thompson, Morrison, Ylin and CAM – perform generally well and have case-dependent strength and weaknesses. Our selection of microphysics schemes therefore includes a diverse set of parametrisations with varying performances. This diversity is particularly advantageous for our sensitivity study, as it enables the identification and analysis of key processes contributing to uncertainties in simulated precipitation. The remaining physical parameterizations incorporated in the simulations are presented in the following list. For land surface and planetary boundary layer processes, the Noah-MP (multi-physics) land surface model and the Yonsei University (YSU) schemes were employed, respectively. The rapid radiative transfer model for general circulation model (RRTMG) was used for long-wave and short-wave radiation. The initial and boundary conditions for this simulation were derived from the ERA5 dataset. Cumulus parameterisation was not utilised. The model employed a total of 50 terrain-following vertical layers, with the model top located at 25 hPa. The simulation of the MCS cases began at 00 UTC on July 14, 2008 and ended at 00 UTC on July 24, 2008. For the snow case, the simulation period spanned from 00 UTC on October 1, 2018 to 00 UTC on October 9, 2018.

2.3. Methods

2.3.1. List and definition of variables

In this work, we examined precipitation rate, θ_e , CAPE, IVT, LWP, IWP and hydrometeors mixing ratios (qcloud, qice, qrain, qsnow, qgraupel, qhail). Precipitation rate was produced by WRF runs and validation datasets. CAPE – defined as the maximum value throughout the atmospheric column – and hydrometeors were simulated by WRF and ERA5. The remaining variables were specifically computed for the analysis.

θ_e was computed using Eq. (1) (Zhou et al., 2009), where T is the air temperature, p is the air pressure, θ is the potential temperature of dry air, q_v is the mixing ratio of water vapour, L is the latent heat of condensation per unit mass and c_p is the specific heat per unit mass at constant pressure of moist air.

$$\theta_e = \theta(T, p) \exp\left(\frac{L q_v}{c_p T}\right) \quad (1)$$

To calculate IVT, we used the horizontal winds (northward component v, eastward component u) and the specific humidity on pressure levels to calculate the zonal and meridional water vapour fluxes q_u and q_v . IVT was then defined as follows (Shen et al., 2021):

$$\text{IVT} = \frac{1}{g} \int_{p_0}^{p_t} \sqrt{(q_u)^2 + (q_v)^2} \, dp \quad (2)$$

where p_t is the model top pressure level at 30 hPa, p_0 is the model bottom pressure level at 975 hPa (875 hPa) for the MCS (snow) event, p is the air pressure, g is the gravity acceleration constant. The pressure levels p_0 have been chosen as the lowest levels for which data were available.

LWP and IWP were computed using Eq. (3) (Chen et al., 2015), where qsum is the sum of liquid (solid) hydrometeors for LWP (IWP) calculations. Specifically, to compute LWP, qsum is equal to the sum of qcloud and qrain in all six WRF simulations and ERA5. For the computation of IWP, qsum is equal to the sum of qice and qsnow in ERA5, CAM and Ylin; to the sum of qice, qsnow and qgraupel in Thompson, Morrison and WDM6; to the sum of qice, qsnow, qgraupel and qhail in WDM7.

$$\text{LWP} = \frac{1}{g} \int_{p_0}^{p_t} \text{qsum} \, dp \quad (3)$$

2.3.2. Statistical tests

We applied three metrics to quantitatively investigate the results. First, we computed correlation coefficients to analyse the hourly temporal evolution of precipitation to assess the performance of WRF simulations and validation datasets.

Second, we computed the fractions skill score (FSS), a neighbourhood-based verification method that evaluates the accuracy of a simulation using an observational dataset as reference (Roberts and Lean, 2008). A main advantage of this method is that it avoids double penalisation for spatial or temporal mismatches and the maximum score can be reached even if the model does not perfectly reproduce the spatiotemporal precipitation pattern. Unlike point-to-point metrics such as root mean square error or spatial correlation, FSS quantifies spatial pattern similarity and is less sensitive to displacement errors, making it more suitable for assessing high-resolution precipitation simulations. We computed two constants for each precipitation threshold: FSSrandom and FSSuniform. FSSrandom represents the fraction of points above the threshold in the reference dataset (IMERG), while FSSuniform defines a benchmark score halfway between FSSrandom and the perfect score. It is defined as FSSuniform = 0.5 + FSSrandom/2 and delineates the minimum score to be reached by a simulation to be considered reasonably skilful. The FSS was computed using Python FSSprob scripts and modules (<https://zenodo.org/records/10518328>).

Lastly, we computed the partial correlation coefficients between time series of precipitation and LWP/IWP to establish which hydrometeor phase dominates precipitation formation. This statistical technique estimates the linear relationship between two variables while accounting for the effect of one or more additional variables. In our work, we first evaluated the correlation between precipitation and LWP while controlling the effect of IWP and then we analysed the correlation between precipitation and IWP while controlling the effect of LWP.

3. Results and discussion

3.1. Precipitation assessment

In the MCS case, most observation-based datasets (IMERG, GLDAS and MSWEP) show consistent temporal evolution and total accumulated precipitation amounts (Fig. 2a-b). The precipitation increased rapidly from July 19, reached a maximum rate of $\sim 20 \text{ mm day}^{-1}$ on July 21, and then decreased until July 23. ERA5 shows similar temporal evolution and total accumulated precipitation values, with delayed increasing and decreasing rates. On the other hand, APHRODITE exhibits a precipitation peak that is about 25 % weaker, which is reflected in its total accumulated precipitation. Despite slight variations in timing and duration of the precipitation peak, ERA5 produces accumulated precipitation values comparable to the first three observation-based datasets. IMERG, MSWEP and APHRODITE show the MCS centred around

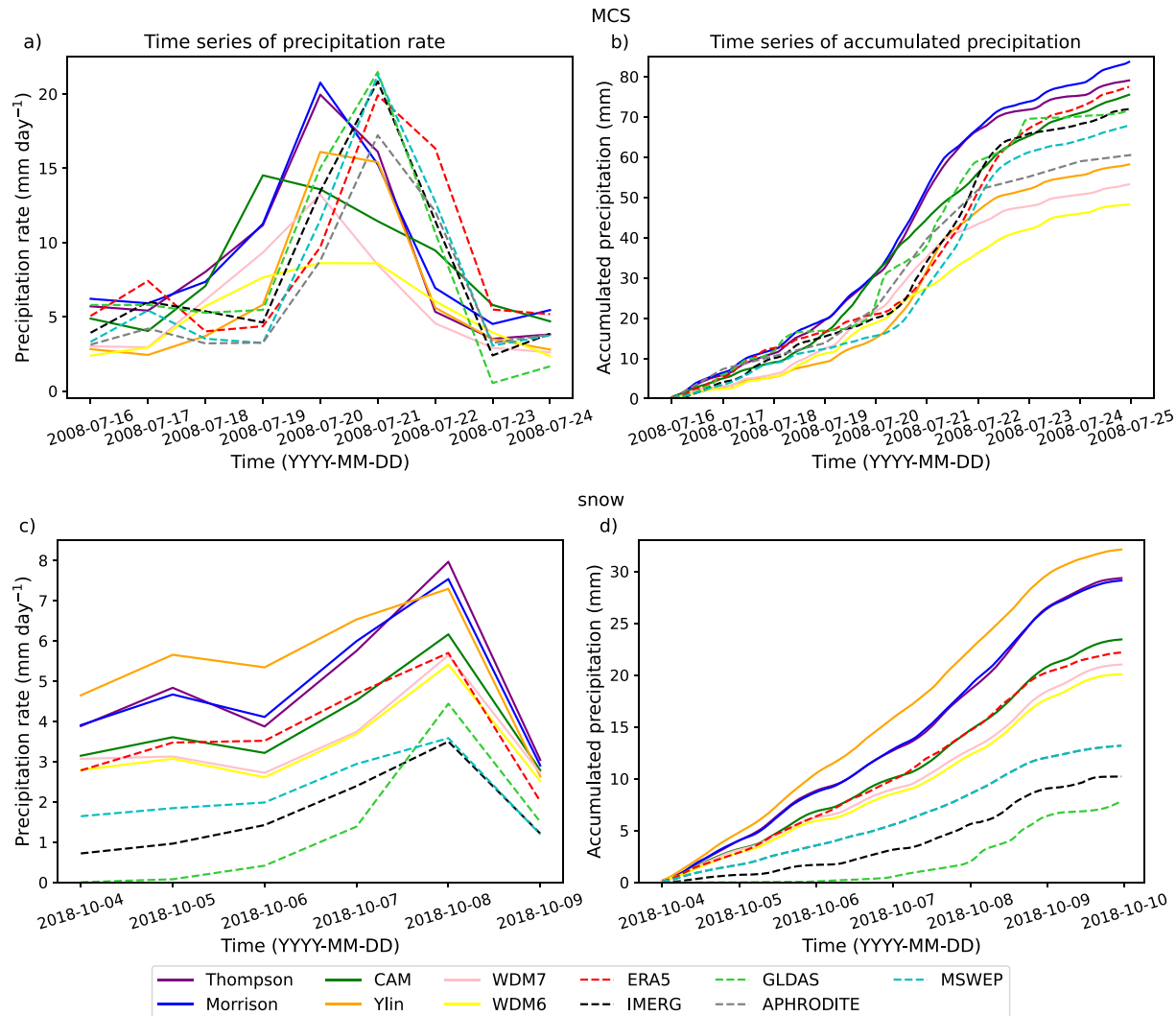


Fig. 2. Time series of a) daily precipitation rate (mm day^{-1}) and b) accumulated precipitation (mm) during the MCS event averaged over latitudes 26–35°N and longitudes 100–114°E. c) Daily precipitation rate (mm day^{-1}) and d) accumulated precipitation (mm) during the snow event averaged over latitudes 27–35°N and longitudes 90–105°. The solid lines represent precipitation rates from the WRF experiments, while the dashed lines represent precipitation rates from observation-based datasets and ERA5 reanalysis.

113°E, while GLDAS displays two weaker precipitation centres near 107°E and 113°E (Fig. S1). ERA5 produces a northeast-southwest-oriented precipitation band in the eastern part of the domain, similar to APHRODITE and IMERG. However, ERA5 also shows a western precipitation centre, as seen in GLDAS and MSWEP. Overall, IMERG and MSWEP exhibit very similar temporal evolution and spatial distribution, while GLDAS and APHRODITE display minor differences in spatial pattern.

In the snow case, all observation-based datasets (IMERG, GLDAS and MSWEP) show similar temporal evolution, reaching a precipitation peak of $\sim 3.5 \text{ mm day}^{-1}$ on October 8 (Fig. 2c). ERA5 displays a comparable precipitation evolution, but with a higher precipitation peak. Compared to observational datasets, its total accumulated precipitation is roughly three times larger (Fig. 2d). IMERG, GLDAS and MSWEP show two precipitation centres at 95°E and 102°E (Fig. S2). However, ERA5 produces additional heavy precipitation regions in the southern TP around 93°E and 102°E. The overestimated precipitation in ERA5 may be resulted from a broader spatial extent of precipitation compared to IMERG, GLDAS and MSWEP (Fig. 3o-p, S2). Overall, IMERG and MSWEP display very similar temporal evolution and spatial distribution, while GLDAS exhibits minor differences in the temporal evolution.

We selected IMERG as reference for the precipitation analysis in both

case studies. Despite some limitations, IMERG shows reliable performance throughout the year over the TP region and provides higher spatiotemporal resolution compared to other observation-based datasets (Kumar et al., 2021; Lyu et al., 2024; Xu et al., 2022). ERA5 is also considered, since it is used as reference in the analysis of precipitation-related factors in the following sections.

In the MCS simulations, the WRF experiments exhibit an earlier and mostly broader peak of precipitation compared to observations and reanalysis (Fig. 2a). Thompson and Morrison produce precipitation intensities closest to those in most validation datasets. Both schemes simulate a peak of $\sim 20 \text{ mm day}^{-1}$ on July 20, about one day earlier compared to observations and reanalysis. The microphysics schemes that reproduce the hourly precipitation rate most similarly to IMERG and ERA5 are Ylin, Thompson, and Morrison, with correlation coefficients of 0.69–0.60, 0.61–0.44, and 0.57–0.45, respectively. Accumulated precipitation is well simulated by Thompson, Morrison, and CAM, whereas the rest of the microphysics schemes underestimate it by up to 40 % compared to observations and reanalysis (Fig. 2b). The precipitation spatial distribution is strongly influenced by topography and the development of the convective system. However, substantial differences emerge depending on the microphysics scheme used (Fig. 3a-h, S1). Potential causes of these discrepancies include the representation

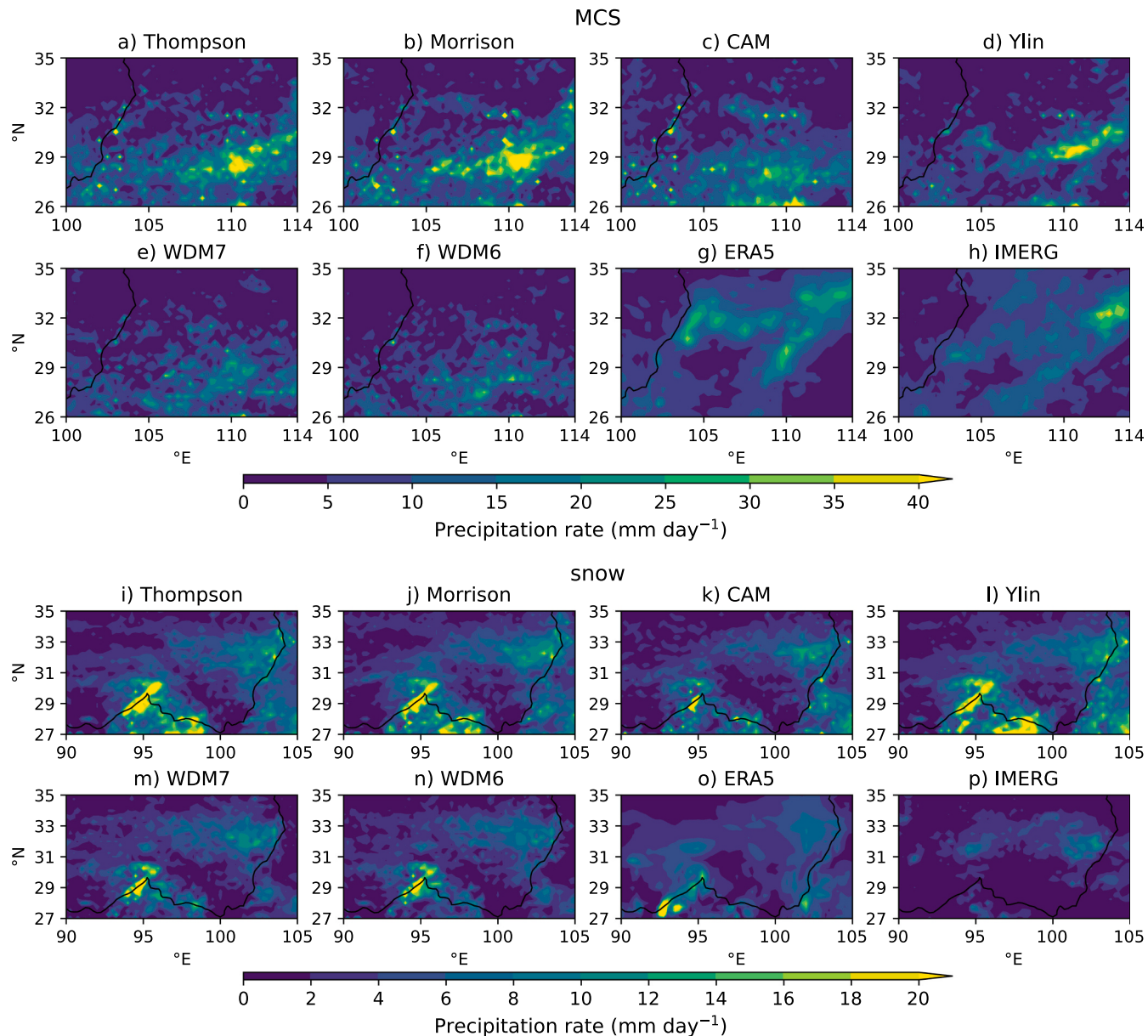


Fig. 3. Spatial distributions of precipitation rate (mm day^{-1}) during the MCS event averaged over 16–24 July, i–p) during the snow event averaged over 4–9 October from the six WRF microphysics schemes, ERA5, and IMERG. ERA5's horizontal grid has been used as reference to remap WRF experiments and IMERG. The black contours indicate elevation at 3000 m.

of convective activity, moisture transport and cloud composition, which are investigated in the next sections of this study. In ERA5, IMERG, Thompson, Morrison, and Ylin, the precipitation peaks are intense and spatially limited over the eastern side of the Sichuan Basin. In contrast, CAM, WDM7, and WDM6 produce weaker and more spatially distributed peaks. All WRF experiments locate the maximum precipitation around 29°N and 110°E , which is shifted towards southwest compared to observational datasets and ERA5.

In the snow simulations, the WRF experiments produce the correct timing but different intensities of precipitation compared to observations and reanalysis. The microphysics schemes WDM7, WDM6, and CAM simulate the closest precipitation maxima to observations and ERA5, reaching a peak of about 6 mm day^{-1} on October 8 (Fig. 2c). CAM, WDM6, and Thompson produce hourly precipitation rates most similar to IMERG and ERA5, with correlation coefficients of $0.85\text{--}0.74$, $0.85\text{--}0.74$, and $0.83\text{--}0.78$, respectively. Accumulated precipitation simulated by CAM, WDM7, and WDM6 are closer to ERA5, while the

remaining simulations overestimate it by up to $\sim 35\%$. The WRF experiments simulate values of accumulated precipitation up to three times larger than IMERG (Fig. 2d). The spatial patterns are dependent on the topography of the area and display major differences in intensity depending on the microphysics scheme. While all WRF experiments and ERA5 produce an intense and limited in space precipitation peak in the western part of the domain, observations exhibit weak precipitation maxima. All WRF microphysics schemes reproduce the main precipitation peak around 29°N and 95°E , located northward compared to ERA5. A minor precipitation peak is shown in all datasets around 32°N and 104°E (Fig. 3i–n, S2). Compared to IMERG and ERA5, WDM7 and WDM6 simulate closely the minor peak in terms of intensity and spatial distribution, while the other microphysics schemes exhibit stronger precipitation located on the southern and eastern slopes of the TP rather than on the plateau itself.

To quantitatively assess the performance of the datasets in reproducing the precipitation field, we computed the FSS for modelled daily

precipitation using IMERG as reference (Fig. 4a-f). As expected, FSS values increase with increasing spatial scales, and decrease with higher precipitation thresholds. For the MCS simulation, the observation-based datasets (GLDAS, APHRODITE and MSWEP) and ERA5 have the highest FSSs across precipitation thresholds and spatial scales. The performance of the six WRF experiments depends heavily on the precipitation thresholds. At lower thresholds (Fig. 4a) Thompson and Morrison are overall the best performing, going over the FSSuniform at spatial scales of 45 km. However, this is not necessarily valid for higher thresholds. A possible explanation is that these two experiments simulate broad regions of light precipitation and capture the observed precipitation centres in the northeastern domain and to the east of the TP (Fig. 3a-b). In fact, with a precipitation threshold of 15 mm day⁻¹, Ylin produces the best performance, and it is the only microphysics scheme that exceeds the FSSuniform at larger spatial scales (Fig. 4c). As shown in Fig. 3d, Ylin produces precipitation over smaller areas compared to other micro-physics runs and datasets, and simulates the heavy precipitation (> 15 mm day⁻¹) centres close to those in IMERG. On the other hand, WDM7, WDM6, and CAM generally show the lowest FSS values due mismatches in the locations of both light and heavy precipitation (Fig. 3c,e,f).

In the snow simulation, the FSS values of observation-based datasets (GLDAS and MSWEP) and ERA5 are lower compared to the six WRF experiments, with the only exception of ERA5 at a 6 mm day⁻¹ precipitation threshold and spatial scales over 40 km (Fig. 4f). On the contrary, WDM7 and WDM6 consistently provide the best performance across precipitation thresholds and spatial scales. With a 2 mm day⁻¹ precipitation threshold, all six WRF microphysics schemes and ERA5 exceed the FSSuniform (Fig. 4d), while with a 6 mm day⁻¹ precipitation threshold, none of the datasets reach the FSSuniform parameter (Fig. 4f). These results are consistent with the precipitation patterns

shown in Fig. 3i-n, where all the WRF simulations generate light precipitation in areas similar to ERA5 and IMERG. However, they all produce heavy precipitation on the southern slope of the TP, which is not found in IMERG. The FSS analysis demonstrates that the best-performing microphysics scheme depends not only on the nature of the precipitation event but also on the precipitation thresholds and spatial scales. Microphysics schemes that accurately simulate the event at smaller spatial scales do not necessarily perform as well over larger scales. Similarly, microphysics schemes that well capture the low-intensity precipitation are not necessarily the best in reproducing intensive precipitation cores.

Multiple studies on the same events (Kukulies et al., 2023b; Lin et al., 2023; Prein et al., 2023) show that varying microphysics scheme in WRF simulations leads to different timing, intensities, and spatial patterns of precipitation, which are found in our results as well. These studies also suggest that Thompson, Morrison, CAM, and Ylin perform equally well and have strengths and weaknesses depending on the case study, whereas WDM7 and WDM6 produce consistently lower-than-average performances. Additional studies (Karki et al., 2018; Orr et al., 2017; Thomas et al., 2021; Zhou et al., 2024) have identified Thompson as the most suitable scheme to reproduce summer precipitation in the TP region compared to other microphysics schemes. Our results partially confirm previous findings, attributing to Thompson and Morrison the best performances in simulating precipitation in the MCS case. On the other hand, WDM7 and WDM6 are shown to give the best performances in the heavy snow system case. This instance emphasises that the performance of the schemes is also dependent on the nature of the precipitation event, and schemes that well simulate summer precipitation can struggle to reproduce snowfall events in autumn and vice versa. Identifying the causes of these discrepancies is complex. Variations in

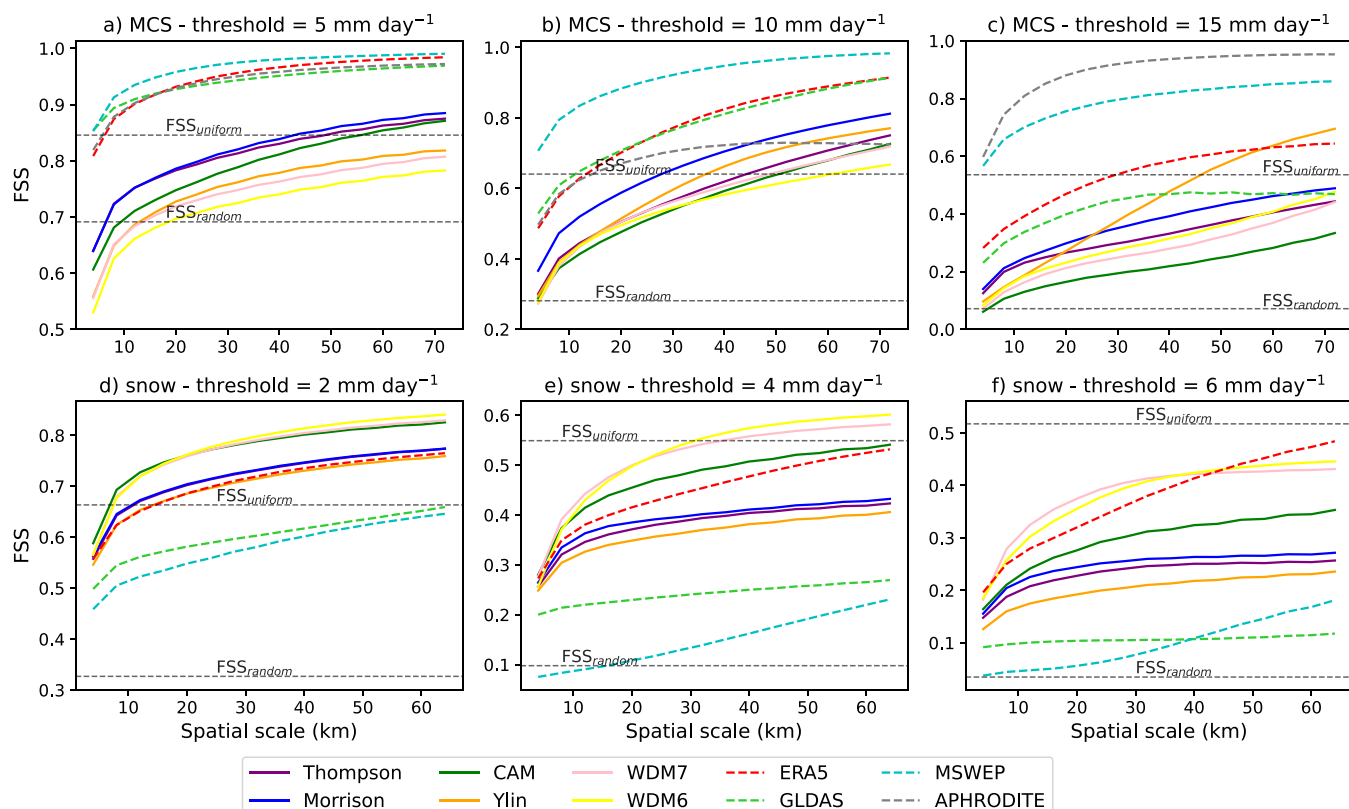


Fig. 4. The fraction skill score (FSS) versus spatial scale for the MCS event using a) 5 mm day⁻¹, b) 10 mm day⁻¹ c) 15 mm day⁻¹ as precipitation threshold. The FSS for the snow event using d) 2 mm day⁻¹, e) 4 mm day⁻¹ f) 6 mm day⁻¹ as precipitation threshold. The solid lines represent the FSS of the six WRF experiments, while the dashed lines represent the FSS of observations and reanalysis datasets. The dashed grey lines indicate the parameters FSSuniform and FSSrandom, which have been defined using IMERG as reference.

the representation of hydrometeors (e.g. their size and distribution) affect thermodynamic processes through phase changes and associated latent heat release, thereby influencing cloud dynamics. These interactions regulate hydrometeor growth and ultimately affect precipitation intensity (Reshma Mohan et al., 2018; Thomas et al., 2021). Prior research on Thompson, Morrison and WDM6 suggests that variations in the description of melting and aggregation processes of solid hydrometeors could explain the differences in simulated precipitation rates (Lim and Hong, 2010; Segele et al., 2013; Zhang and Schultz, 2024). A study over western Himalayas indicates the snow size distribution as another potential cause for differences in precipitation simulations. For instance, in the Thompson scheme, snow size distribution depends on ice water content and temperature. It is described as a sum of exponential and gamma distributions, with snow particles of non-spherical shape. This contrasts with other schemes that assume spherical snow shape and constant density. These differences affect the way the schemes treat water phase changes and precipitation (Tiwari et al., 2018). Another factor contributing to precipitation variability could be aerosol-cloud-radiation interactions. Their description in the microphysics schemes influences the concentrations, size and lifetime of the cloud droplets by altering the cloud condensation nuclei and enhancing shortwave heating and longwave cooling effects (De Meij et al., 2018). However, rather than identifying sources of uncertainty within the microphysics description of the schemes, our aim is to establish which precipitation-related atmospheric processes are affected by the choice of microphysics scheme and understand how these discrepancies impact the overall precipitation simulation. Our analysis has revealed differences in the temporal evolution of precipitation - specifically in the intensity and width of the peaks – as well as in the total accumulated precipitation amounts and the location of heavy precipitation centres. In the following three sections, we examine convective activity, moisture transport, and cloud composition to clarify their roles in precipitation simulation and to identify connections between specific factors and the exposed uncertainties.

3.2. Convective activity

In this section, θ_e and CAPE are analysed to understand how the representation of convective activity can influence the simulated precipitation. During the MCS case, the vertical profile of θ_e suggests varying atmospheric stability at different levels (Fig. 5a). The θ_e from ERA5 and WRF experiments mostly agree, except near the surface where

WRF θ_e values are higher of about 10 K compared to ERA5 θ_e values. In addition, microphysics schemes that simulate higher (lower) θ_e throughout the atmosphere, namely Thompson and Morrison (WDM7 and WDM6), also produce higher (lower) total accumulated precipitation. Below 650 hPa the θ_e sharply decreases with height, suggesting a strongly unstable environment. This indicates that warm moist air is below cooler drier air, creating favourable conditions for deep convective activity. Between 650 hPa and 500 hPa the θ_e gradient turns positive, suggesting increasing atmospheric stability and limited further convective development. Above 500 hPa θ_e values continue to increase with height, indicating stable conditions and weak or no convective updrafts.

During the snow event, the θ_e vertical profile shows an overall stable atmosphere, with lower values compared to the MCS case that indicate weaker convective activity (Fig. 5b). The θ_e from ERA5 and WRF experiments mostly agree, except below 600 hPa where θ_e from ERA5 exhibits a sharper negative slope. Similarly to the previous case, microphysics schemes that simulate higher (lower) θ_e throughout the atmosphere, namely Ylin, Thompson and Morrison (WDM7 and WDM6), also produce higher (lower) total accumulated precipitation. In the WRF experiments, the θ_e stays roughly constant below 400 hPa, indicating a weakly stable lower atmosphere and less likelihood of strong convection as vertical mixing is limited. Above 400 hPa θ_e values increase sharply, suggesting a more stable environment.

CAPE is also closely related to precipitation formation and provides valuable insights into the atmospheric instability during the events. Our MCS simulations show that CAPE reaches its highest values about two days before precipitation peak and its lowest during the peak (Fig. 6a). The microphysics schemes that report relatively high (low) CAPE values, namely Thompson and Morrison (WDM7 and WDM6), also simulate the most intense (weak) precipitation peaks. In the snow simulations, the relationship between CAPE and precipitation intensity is still valid (Fig. 6b), even though CAPE values are about ten times smaller than in the MCS case and do not exhibit a clear maximum prior to the event. Interestingly, the WRF experiments produce the CAPE values two to three times smaller than ERA5 in both events.

Among various aspects of cloud microphysics in the simulation of storm thermodynamics, high θ_e and CAPE associated with large-scale environments are key indicators in identifying MCSs (Shukla et al., 2022). Several studies about heavy precipitation events present similarities to our work, showing that Thompson and Morrison simulate higher θ_e compared to other microphysics schemes and lead to more

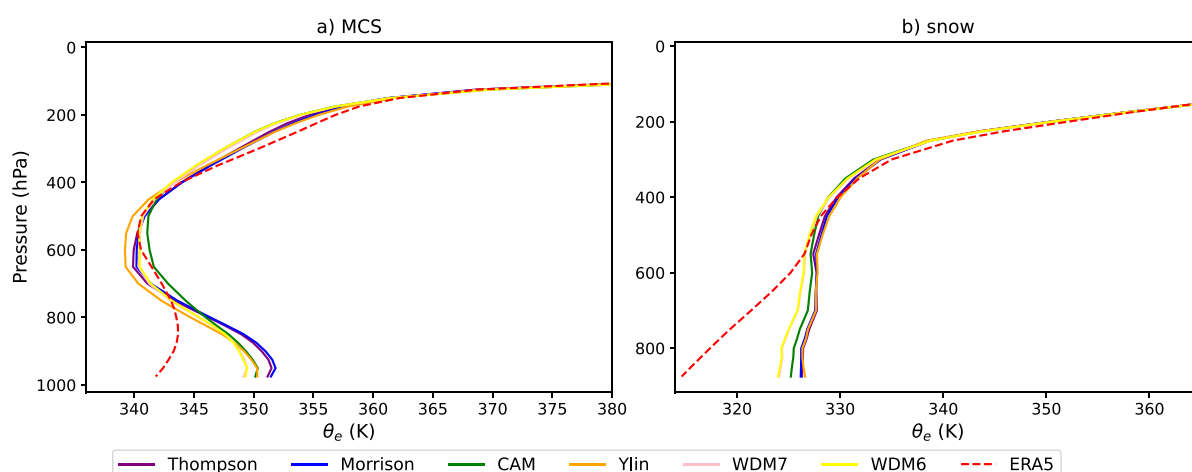


Fig. 5. Vertical profiles of the equivalent potential temperature θ_e (K) a) during the MCS case averaged over 16–24 July, latitudes 26–35°N and longitudes 100–114°E, and b) during the snow event averaged over 4–9 October, latitudes 27–35°N and longitudes 90–105°E. The solid lines represent θ_e from the six WRF experiments, while the dashed red lines represent θ_e from ERA5. (For interpretation of the references to colour in this figure legend, the reader is referred to the web version of this article.)

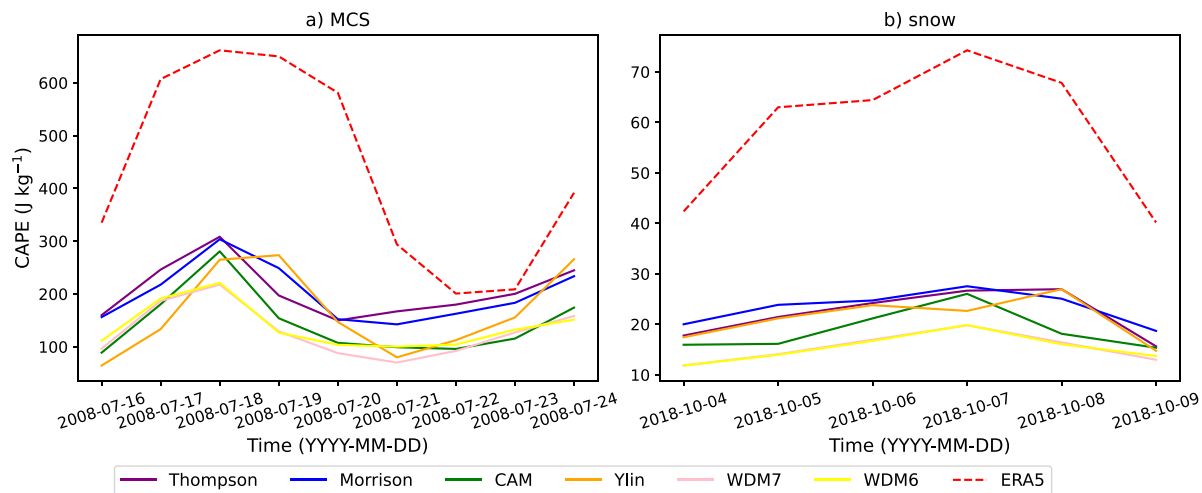


Fig. 6. Time series of daily convective available potential energy CAPE (J kg^{-1}) a) during the MCS event averaged over latitudes 26–35°N and longitudes 100–114°E, and b) during the snow event averaged over latitudes 27–35°N and longitudes 90–105°E. CAPE is defined as the maximum value throughout the atmospheric column. The solid lines represent CAPE from the six WRF experiments, while the dashed red lines represent CAPE from ERA5. (For interpretation of the references to colour in this figure legend, the reader is referred to the web version of this article.)

intense precipitation (Feng et al., 2018; Karki et al., 2018; Reshma Mohan et al., 2018). Other studies also report that Thompson and Morrison produce higher CAPE values compared to other microphysics schemes (Podet et al., 2020; Reshma Mohan et al., 2018; Thomas et al., 2021). Our findings indicate that, in both case studies, the θ_e is a reliable indicator of atmospheric instability and discrepancies in its values among microphysics schemes can be related to the total accumulated precipitation. Moreover, also CAPE is a valid indicator of atmospheric instability and its intensity and timing can be associated with the intensity and timing of precipitation rates in different WRF experiments.

3.3. Moisture transport

Moisture is a crucial component in the formation of precipitation, as it provides the necessary water vapour that condenses into clouds and ultimately falls as precipitation. We examined the horizontal moisture transport simulated by different microphysics schemes and compared the model output with ERA5. In the MCS case, ERA5 produces the strongest northward IVT compared to the WRF simulations, with values above $400 \text{ kg m}^{-1} \text{s}^{-1}$ on the southeastern side of the domain (.

Fig. 7g). The negative differences in IVT intensity between the WRF simulations and ERA5 could explain the south-westward shift of precipitation peaks in the WRF experiments compared to ERA5, likely due to the WRF model's limitation in accurately capturing the TPV (Kukulies

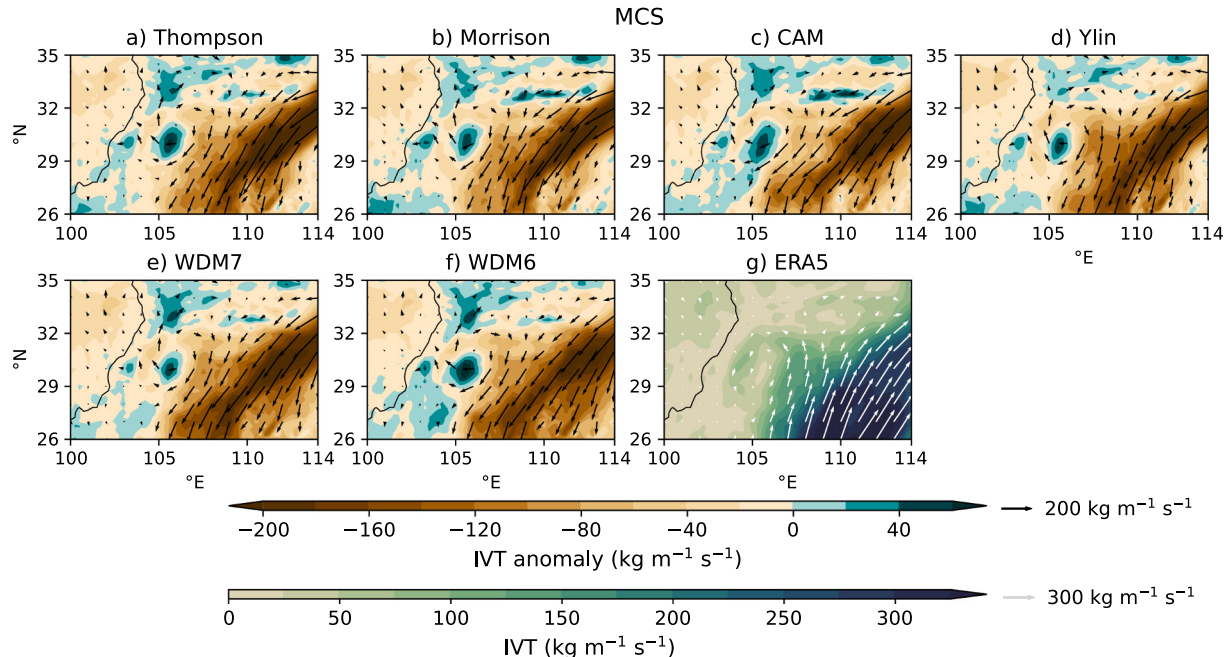


Fig. 7. Spatial distributions of a)-f) vertically integrated water vapour transport IVT ($\text{kg m}^{-1} \text{s}^{-1}$) differences of six WRF simulations – ERA5 and g) IVT of ERA5 for the MCS event averaged over 16–24 July. The black contours indicate elevation at 3000 m. The white arrows indicate the direction of IVT, while the black arrows indicate the direction of IVT anomaly. The reference intensities of $300 \text{ kg m}^{-1} \text{s}^{-1}$ and $100 \text{ kg m}^{-1} \text{s}^{-1}$, respectively, are shown beside the colorbars.

et al., 2023b). Examining the microphysics schemes individually reveals differences in IVT intensity and direction, with variations up to 15 % in absolute IVT intensity. These differences can be linked to variations in precipitation intensity and location. For instance, by comparing the extent of the negative anomaly in Thompson and Morrison with WDM7 and WDM6 over the eastern side of the Sichuan Basin, we notice that the former two microphysics schemes produce stronger IVT towards northeast than the latter two (Fig. 7a-f). This is reflected in the intensity and location of heavy precipitation centres, which are stronger and more shifted towards northeast in Thompson and Morrison than in WDM7 and WDM6. Overall, microphysics schemes with stronger (weaker) IVT towards northeast also exhibit higher (lower) precipitation rates and stronger (weaker) shifts of heavy precipitation centres towards northeast.

In the snow case, ERA5 produces the weakest IVT from the southwest compared to other simulations, with peaks around $100 \text{ kg m}^{-1} \text{s}^{-1}$ in the low-elevation areas of the domain (Fig. 8g). The positive discrepancies in IVT intensity between the WRF experiments and ERA5 in the south and along the eastern border of the TP may explain why the precipitation peaks are shifted towards northeast in the WRF experiments compared to the reanalysis dataset. In addition, the abundant IVT from the south in the WRF simulations also results in more precipitation along the southern and eastern boundaries of the TP. Similarly to the previous case, the microphysics schemes lead to differences in IVT intensity and direction towards northeast, with variations of up to 20 % in absolute IVT intensity. These differences can be associated with changes in the intensity and location of precipitation. For instance, by comparing the extent of the positive anomaly in WDM7 and WDM6 with Thompson and Ylin over low-elevation areas in the south and over high elevation areas in the northeast, we notice that the first two microphysics schemes produce weaker IVT towards northeast compared to the latter two (Fig. 8a-f). This is reflected in the intensity and location of heavy precipitation centres, which are weaker and less shifted towards northeast in WDM7 and WDM6 than in Thompson and Ylin. These results consistently suggest that the microphysics schemes could affect the large-scale IVT and the location as well as intensity of precipitation centres.

To complete the analysis, we examined the vertical moisture transport. In both case studies, the timing and intensity of the vertical moisture transport are consistent with the timing and intensity of

precipitation maxima: microphysics schemes that simulate weaker (stronger) vertical moisture transport also produce weaker (stronger) precipitation peaks (Fig. S5, S6).

Understanding the intricate relationship between moisture flux and precipitation remains a challenge due to inadequate observational data and complex terrain. Other factors influencing the overall performance include the resolution of the model and its ability to correctly reproduce the wind field (Lin et al., 2023). A simulation study carried out for two summer months over central TP suggests that Thompson performs well in reproducing local precipitation and moisture processes compared to other microphysics schemes (Lv et al., 2020). Previous studies on summer precipitation over the Himalayas report large differences in horizontal moisture transport between Thompson, Morrison, Ylin and WDM6 schemes, which affect cloud formation and precipitation intensity and location (Orr et al., 2017; Zhou et al., 2024). Thompson and Morrison consistently simulate stronger moisture transport from the south, while Ylin and WDM6 produce weaker transport. By comparing WRF experiments against observation-based datasets, these studies conclude that Morrison and Thompson deliver the best performance, Ylin performs moderately well, and WDM6 performs the worst. Our findings mostly agree with previous research but also indicate that the performance of microphysics schemes depends on the nature of the events, as the best performing microphysics schemes in one case study are not necessarily the best in the other.

3.4. Cloud composition

Variations in hydrometeors contribution to precipitation depend on how cloud and precipitation microphysics are described in the different schemes, and represent an important aspect when examining precipitation. Therefore, we investigated the simulated liquid and solid hydrometeors for both case studies. In the MCS case, the peaks of LWP and IWP occur at the same time (July 20–21) and over the same areas (29°N and 110°E) as the precipitation peaks in all WRF experiments and ERA5 (Fig. 9h). However, the magnitudes of LWP and IWP are not proportionate to the magnitude of precipitation (Fig. 9h, S3, 2a), indicating that microphysics schemes that produce higher LWP/IWP values are not necessarily the microphysics schemes producing more intense precipitation. For instance, Thompson and Morrison produce the strongest precipitation peak but not the highest LWP and IWP peaks. On the other

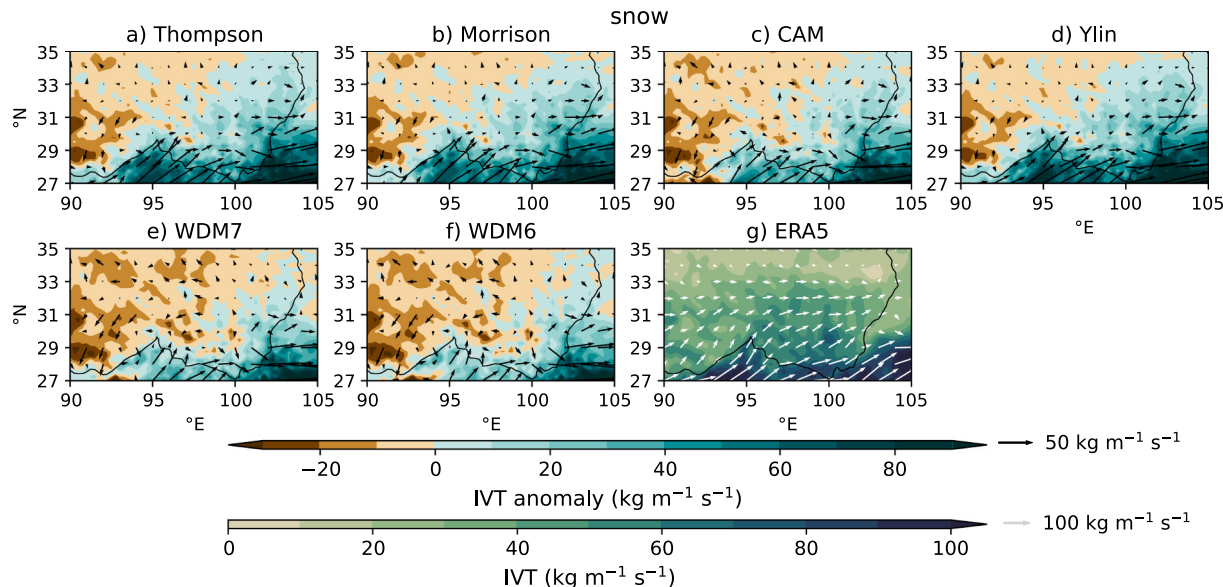


Fig. 8. Spatial distributions of a)-f) vertically integrated water vapour transport IVT ($\text{kg m}^{-1} \text{s}^{-1}$) differences of WRF simulations – ERA5 and g) IVT from ERA5 for the snow event averaged over 4–9 October. The black contours indicate elevation at 3000 m. The white arrows indicate the direction of IVT, while the black arrows indicate the direction of IVT anomaly. The reference intensities of $100 \text{ kg m}^{-1} \text{s}^{-1}$ and $50 \text{ kg m}^{-1} \text{s}^{-1}$, respectively, are shown beside the colorbars.

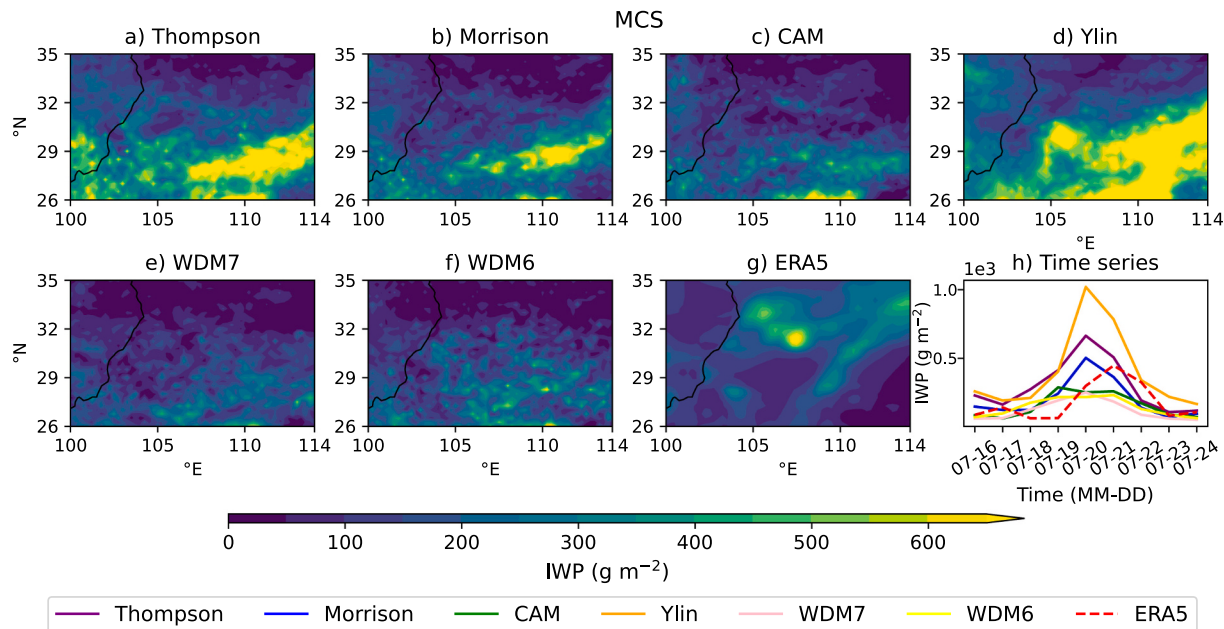


Fig. 9. Spatial distributions of ice water path IWP (g m^{-2}) from a)-f) the six WRF simulations and g) ERA5 for the MCS event averaged over 16–24 July. The black contours indicate elevation at 3000 m. h) Time series of daily IWP for the MCS event averaged over latitudes 26–35°N and longitudes 100–114°E. The solid lines represent IWP from the six WRF experiments, while the dashed red line represents IWP from ERA5. (For interpretation of the references to colour in this figure legend, the reader is referred to the web version of this article.)

hand, CAM and Ylin do not simulate the strongest precipitation peak but simulate the highest LWP and IWP peaks, respectively. The temporal partial correlation between precipitation and LWP/IWP suggests that, in all datasets but Ylin, the evolution of precipitation could be linked to the temporal evolution of solid water content (Table 2). This indicates that IWP may play a more important role than LWP in the MCS case. However, the contribution of liquid species to precipitation is not negligible: in Thompson, CAM and Ylin experiments the correlation coefficients are all above 0.5.

In the snow case, the magnitudes and locations of LWP (Fig. S4) do not align with the spatiotemporal patterns of precipitation (Fig. 2c-d, Fig. 3i-n), whereas the IWP patterns agree with those of precipitation (Fig. 10). Specifically, IWP peaks occur on 8 October at 27°N and 95°E, matching the timing and location of precipitation maxima in all WRF simulations and ERA5. In contrast, LWP peaks do not coincide with precipitation peaks in any dataset. As in the previous case, the average magnitude of LWP and IWP is not proportionate to the intensity of precipitation. The temporal partial correlation of precipitation and LWP/IWP suggests that in all microphysics schemes the driving factor behind precipitation formation may be the content of solid water species. While the contribution of liquid and solid water contents to precipitation varies depending on the microphysics scheme and the nature of the precipitation event, solid hydrometeors dominate overall (Table 2).

The analysis of LWP and IWP can help improve the accuracy of precipitation simulations (Chen et al., 2015, 2016). A sensitivity study of summer 2018 over the TP suggests that the spatial distribution of vertically integrated water vapour (VIWV) closely resembles that of

precipitation in most microphysics schemes. They found that Morrison and Ylin produce higher VIWV and precipitation compared to Thompson, particularly in the southern TP (Zhou et al., 2024). Discrepancies among microphysics schemes could be due to parameters involved in precipitation formation, such as hydrometeor conversion. The ability of the schemes to convert non-precipitable to precipitable water species could also act as a relevant contribution (Shen et al., 2021). Various studies (Martínez-Castro et al., 2019; Tang et al., 2019) report that warm-rain processes have a minor role in the direct formation of precipitation over the TP. However, they regulate the occurrence of supercooled water droplets, which are necessary for the formation of ice nuclei and contribute to precipitation development. Previous research on a MCS over the Tropical Western Pacific reveals that Thompson and Morrison display overall differences in their precipitation simulation. It was found that the main source of uncertainty is linked with solid hydrometeors and related processes (Van Weverberg et al., 2013). Another sensitivity study carried out over the Hanjiang River Basin suggests that precipitation during summer is very sensitive to solid-phase hydrometeors processes (Yang et al., 2021). Our partial correlation results reveal that different microphysics schemes simulate cloud properties and precipitation formation processes differently, leading to major discrepancies in the model output, and can be identified as relevant sources of uncertainty. Overall, solid-phase hydrometeors seem to play a bigger role. Microphysical processes are recognized as crucial for cloud formation as well as in shaping the spatial distribution and intensity of precipitation (Bryan and Morrison, 2012; Kukulies et al., 2023a). However, the influence of microphysical processes has been largely overlooked in previous studies of extreme precipitation events over the

Table 2

Partial correlation coefficients of hourly precipitation and liquid water path, ice water path (LWP, IWP) with p -value ≤ 0.01 . Coefficients with p -values > 0.01 have been marked with an asterisk.

	ERA5	Thompson	Morrison	CAM	Ylin	WDM7	WDM6
MCS: P-LWP	0.24	0.53	0.19	0.64	0.66	0.46	0.13*
MCS: P-IWP	0.66	0.61	0.59	0.89	0.40	0.57	0.58
snow: P-LWP	-0.29	-0.09*	0.12*	-0.01*	0.01*	-0.06*	-0.17*
snow: P-IWP	0.41	0.59	0.63	0.37	0.30	0.58	0.63

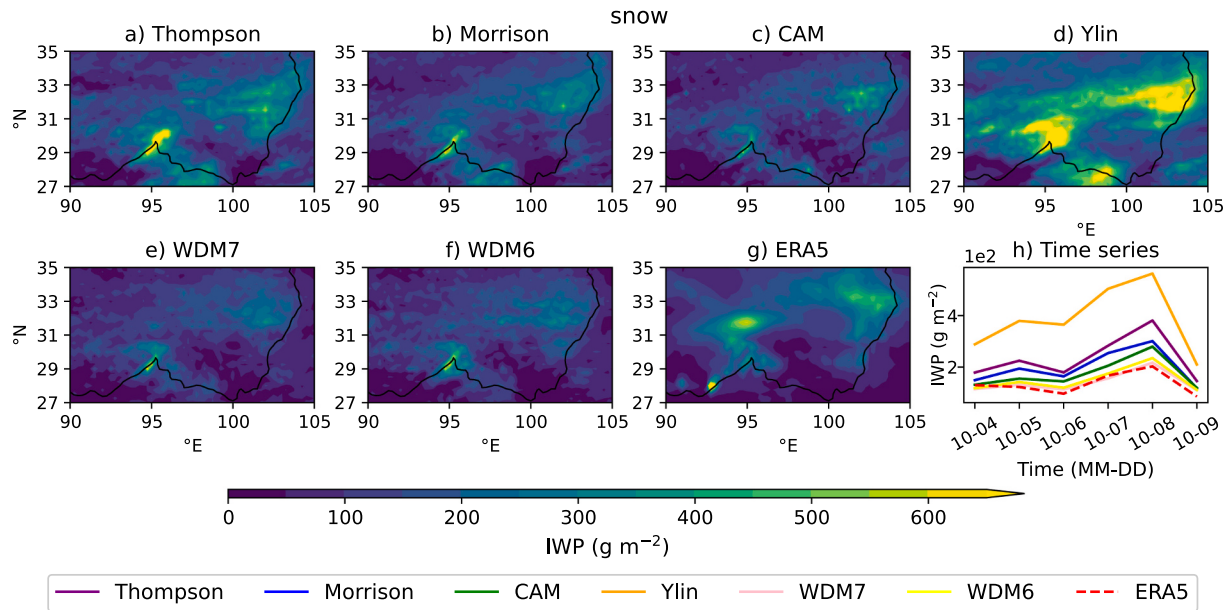


Fig. 10. Spatial distributions of ice water path IWP (g m^{-2}) from a-f) the six WRF simulations and g) ERA5 for the snow event averaged over 4–9 October. The black contours indicate elevation at 3000 m. h) Time series of daily ice water path (IWP) for the snow event averaged over latitudes 27–35°N and longitudes 90–105°E. The solid lines represent IWP from the six WRF experiments, while the dashed red line represents IWP from ERA5. (For interpretation of the references to colour in this figure legend, the reader is referred to the web version of this article.)

TP region.

To address this gap, we analyse the simulated vertical profiles and temporal evolution of hydrometeors mixing ratios. In both case studies, ERA5 produces the highest content of cloud ice and the lowest content of rain. Cloud water and snow by ERA5 are mostly consistent with those in the WRF experiments (Fig. 11).

In the MCS case, simulated cloud water and rain generally peak concurrently with precipitation, although their intensity varies among WRF experiments (Figs. S7, S8). Simulated cloud ice increases during precipitation peaks but exhibits large variability in magnitude and vertical extent, with Thompson and Ylin producing only small amounts (Fig. 12). Snow dominates the hydrometeor mass by one order of magnitude. However, its intensity differs depending on the microphysics scheme, with WDM7 and WDM6 producing the smallest amounts (Fig. 13). Graupel, absent in CAM and Ylin, peaks one to two days before maximum precipitation (Fig. S9). Hail, present only in WDM7, aligns with precipitation peaks timing (Fig. S10). In the snow event, simulated cloud water shows no consistent relation to precipitation, and simulated cloud ice temporal evolution corresponds with precipitation only in some experiments, displaying strong variability across schemes (Fig. 12). Rain and snow generally follow precipitation timing, displaying consistent vertical extents but large variability in magnitude (Fig. 13). Similarly to the previous case, snow is the most abundant hydrometeor but it is underestimated by WDM7 and WDM6. Graupel and hail exhibit similar trends to those seen during the MCS event (Figs. S9, S10).

These findings align with previous studies, which report that Thompson and Morrison simulate similar cloud water, while Thompson yields significantly less cloud ice (Orr et al., 2017; Podeti et al., 2020; Reshma Mohan et al., 2018). Snow stands out among solid-phase hydrometeors with values roughly one order of magnitude greater, highlighting the importance of aggregation processes in cloud development and their critical influence on precipitation outcomes (Martínez-Castro et al., 2019; Tiwari et al., 2018). Thompson produces more snow than Morrison, likely due to its formulation of snow size distribution as a function of ice water content and temperature, whereas Morrison assumes spherical snow particles with constant density. Furthermore, Morrison generates larger snow crystals due to excessive self-

aggregation, driven by an unrealistic collection efficiency (Zhang et al., 2024). Our findings suggest that discrepancies in the representation of hydrometeors across different microphysics schemes can lead to substantial variability among simulations of extreme precipitation. This highlights the need to improve cloud microphysics parameterizations, particularly for solid-phase species, to enhance the accuracy of precipitation modelling.

3.5. Uncertainties and limitations

Observation-based datasets of precipitation, both from ground stations and satellites, face numerous challenges over the TP region due to its complex topography and harsh winter conditions (Jiang et al., 2023). Rain gauge observations over the TP region contain significant uncertainties due to inadequate sampling (Ouyang et al., 2021). Satellite-based observations struggle in detecting snowfall and dealing with thick cloud cover, which hinders precipitation measurements. Additionally, the low reflectance of snow at certain satellite wavelengths further complicates detection (Xu et al., 2022). Differences among gridded observational datasets are large source of uncertainties over the TP (Prein et al., 2023). To address these limitations, we compare multiple precipitation products derived from ground-based, satellite-based, and reanalysis sources.

Another concern to be addressed is the choice of the extreme precipitation events and the domain used for the simulations. The size and location of domain D1 were chosen following the approach of Kukulies et al. (2023b). Domain D1 was designed as a compromise between maximizing the representation of the TP topography and minimizing domain size to limit computational requirements. The choice to analyse two precipitation events was primarily determined by the selection of experiments available within the CORDEX Flagship Pilot Study CPTP and our limited computational resources. The case studies selected by the CPTP project are associated with relevant meteorological phenomena over the TP and represent various weather conditions (Prein et al., 2023). We examined the MCS and the snow system events because of their unique setup and scientific significance. We acknowledge the inclusion of additional case studies as a direction to further assess and expand the current work. Nevertheless, the analysis of targeted case

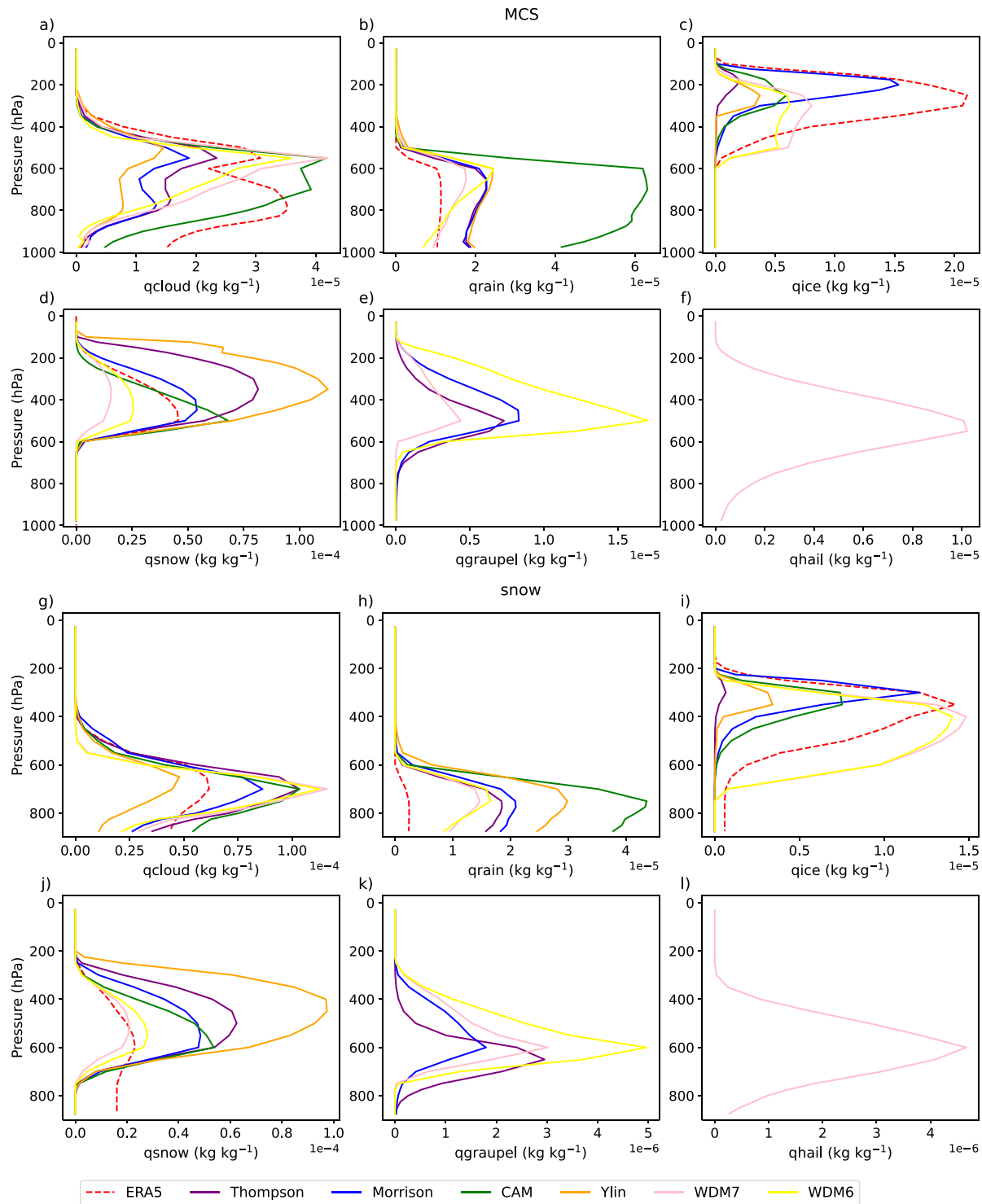


Fig. 11. Vertical profiles of mixing ratios of hydrometeors (kg kg^{-1}) for a-f) MCS event averaged over 16–24 July, latitudes 26–35°N and longitudes 100–114°E, g-l) snow event averaged over 4–9 October, latitudes 27–35°N and longitudes 90–105°E. The solid lines represent the mixing ratios of hydrometeors from the WRF experiments, while the dashed red lines represent the mixing ratios of hydrometeors from ERA5 reanalysis. (For interpretation of the references to colour in this figure legend, the reader is referred to the web version of this article.)

studies remains valuable and widely used to understand complex physical processes (e.g. Gao et al., 2018; Hou et al., 2020; Karki et al., 2018; Lin et al., 2023; Orr et al., 2017; Prein et al., 2023) and provides a foundation for future research. Our results can serve as a first step towards improving cloud microphysics parametrisation to better simulate extreme precipitation events over the TP region.

Lastly, we discuss the choice of studying the influence of cloud microphysics schemes on extreme precipitation events as an integrated outcome of convective activity, moisture transport, and hydrometeor representation. While microphysics schemes are a major driver of uncertainties in simulating precipitation over the TP region, they are not the only one (Prein et al., 2023). Our results could be expanded by

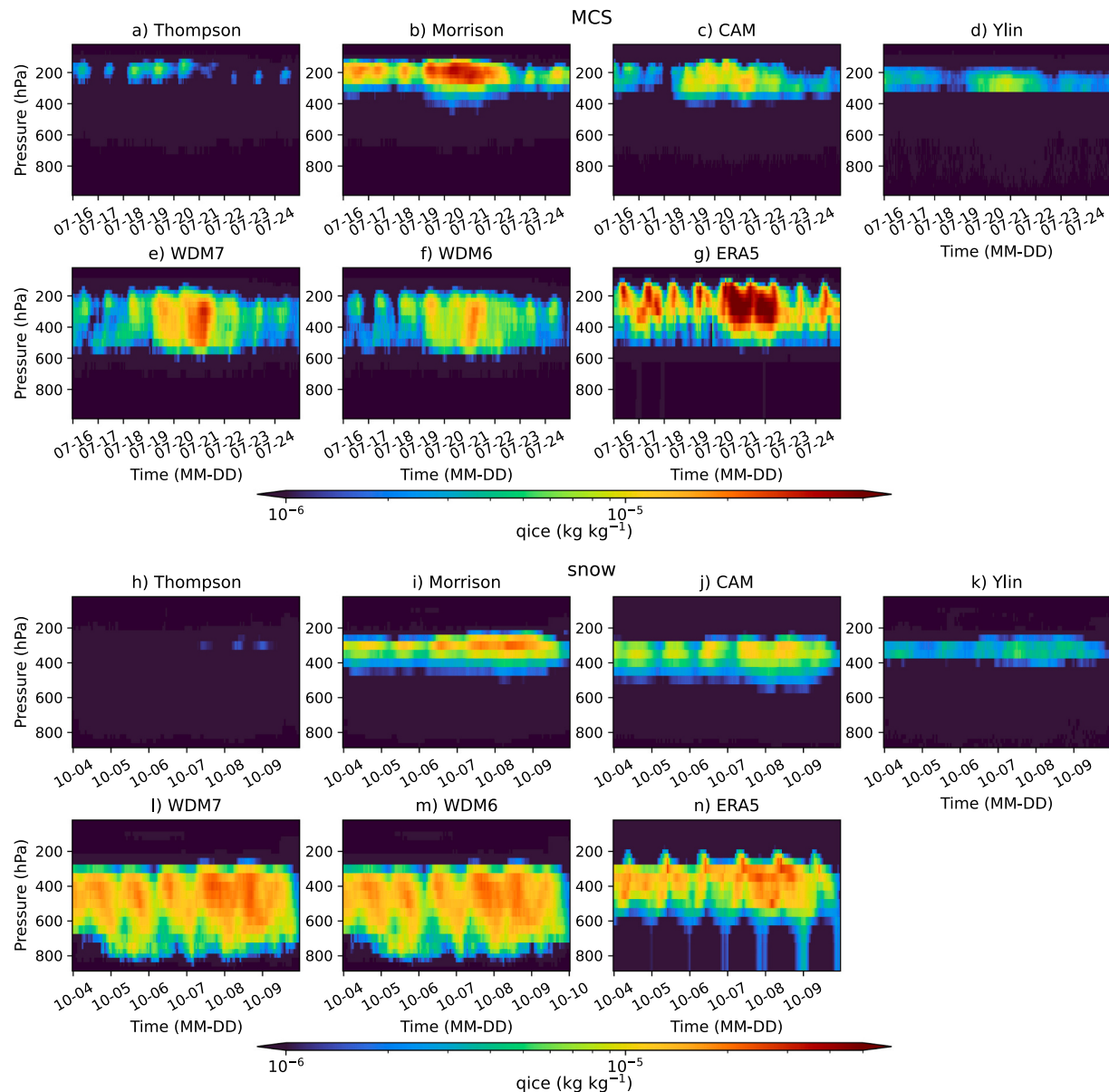


Fig. 12. Temporal evolution of mixing ratio of cloud ice q_{ice} (kg kg^{-1}) a-g) for the MCS event averaged over latitudes 26–35°N and longitudes 100–114°E, h-n) for the snow event averaged over latitudes 27–35°N and longitudes 90–105°E.

performing sensitivity studies on other relevant physical parametrisations, such as shallow convection schemes (Liu et al., 2024). Moreover, assessing the quantitative contributions of convective activity, moisture transport, and hydrometeor representation to precipitation uncertainty is a critical question for improving model performance. Although our results highlight noticeable scheme-dependent differences in convective structure, moisture convergence, and precipitation intensity, attributing a leading role to any single factor would require additional targeted experiments.

4. Conclusions

In this study we used six different cloud microphysics schemes in the state-of-the-art WRF model to simulate two extreme precipitation events over the TP region: a summer MCS in 2008 and a heavy snow system in autumn 2018. First, we assessed the discrepancies in temporal and spatial patterns of precipitation due to the choice of cloud microphysics scheme. Then, we investigated precipitation-related atmospheric processes by analysing the atmospheric instability, moisture transport and

hydrometeors distributions. Finally, we identified key factors leading to modelling uncertainties. Where possible, our simulations were evaluated against observation-based and reanalysis datasets.

The key findings are the following:

1. The choice of cloud microphysics scheme leads to major differences in precipitation spatial distribution and intensity, resulting in variations of accumulated precipitation up to ~40 % of the total amount. In the MCS case WRF experiments reproduce the precipitation peak 1–2 days earlier than validation datasets, while in the heavy snow system case the timing is simulated consistently across schemes.
2. Convective activity representation heavily affects precipitation simulation. Differences in θ_e and CAPE between the microphysics schemes are linked with discrepancies in precipitation intensity and timing as well as the total accumulated precipitation amounts.
3. Biases in horizontal water vapour transport due to microphysics schemes are linked to both the intensity and location of the precipitation peaks. In both case studies, Thompson and Morrison produce stronger IVT compared to WDM7 and WDM6, resulting in more

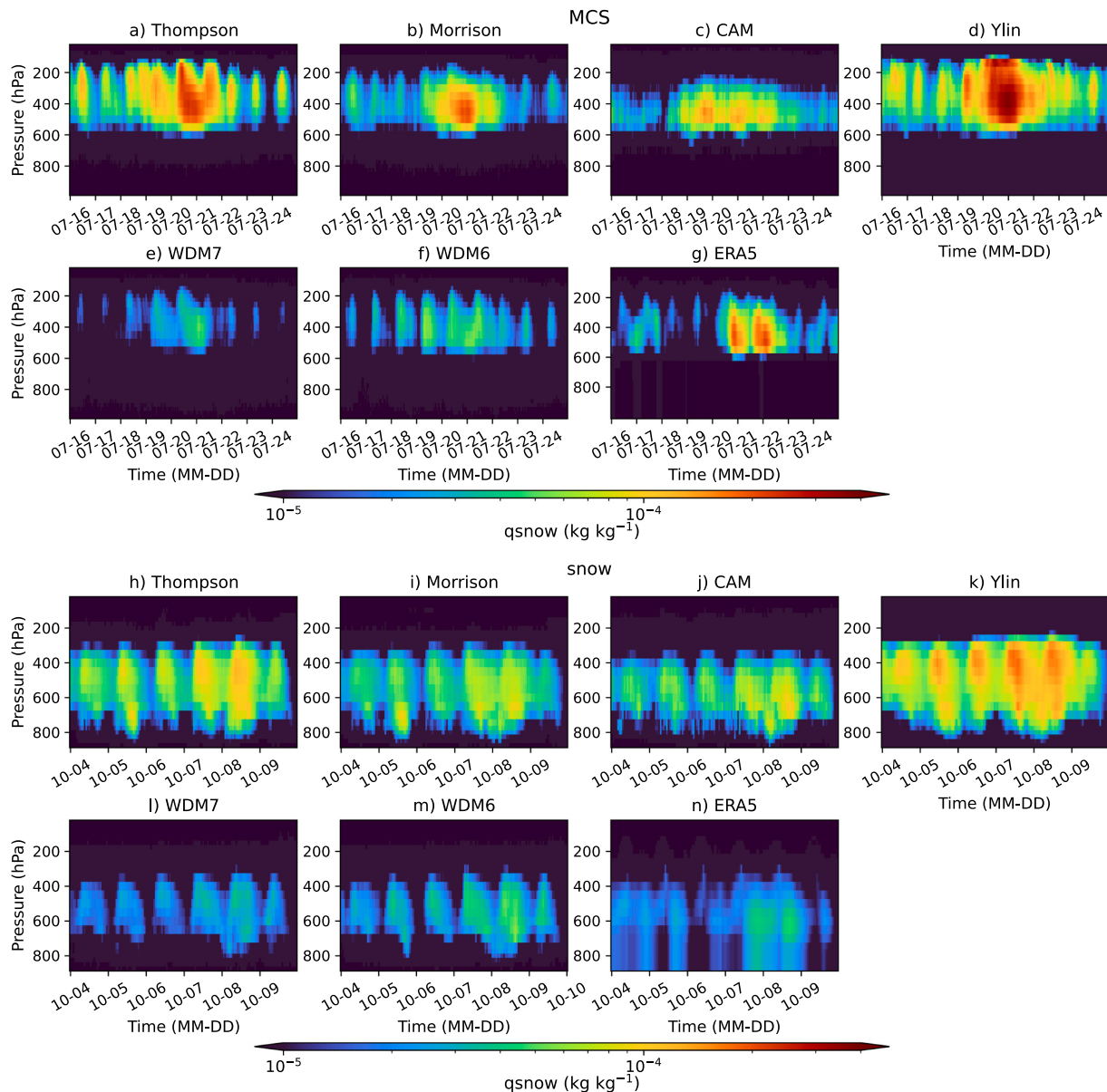


Fig. 13. Temporal evolution of mixing ratio of snow $qsnow$ (kg kg^{-1}) a-g for the MCS event averaged over latitudes 26–35°N and longitudes 100–114°E, h-n) for the snow event averaged over latitudes 27–35°N and longitudes 90–105°E.

- intense precipitation in the former. Moreover, compared to ERA5, WRF experiments show precipitation location shifts that correspond to the strength of northward IVT, with weaker IVT linked to southward shifts and stronger IVT to northward shifts.
4. The impact of liquid- and solid-phase hydrometeors on precipitation formation varies depending on the microphysics scheme and the nature of the precipitation event. In both cases, partial correlation analysis reveals that ice water content is the main contributor to precipitation formation. The representation of hydrometeors – particularly solid-phase species – is likely a key contributor to discrepancies in the intensity, timing, and distribution of simulated precipitation peaks.
 5. Overall, Thompson and Morrison perform best in the MCS case, closely matching validation datasets in terms of timing, magnitude and location of precipitation. In the snow case CAM, WDM7, and WDM6 show better performance in reproducing the magnitude and location of precipitation, as all microphysics schemes simulate the timing consistently.

Our results suggest that improving the simulation of extreme precipitation over the TP region requires careful selection of cloud micro-physics schemes, as they substantially affect the timing, intensity, and spatial distribution of precipitation. Better representation of convective processes, moisture transport, and phase-dependent hydrometeor processes can help reduce modelling uncertainties.

This work could be expanded by including additional precipitation events, as well as other variables and relevant processes that have not been considered so far. Moreover, it would be highly beneficial to analyse specific diagnostics of microphysical process rates for hydrometeors in different schemes and explore how these characteristics relate to our results.

CRediT authorship contribution statement

Irene Elisa Bellagente: Writing – review & editing, Writing – original draft, Visualization, Methodology, Formal analysis, Data curation, Conceptualization. **Hui-Wen Lai:** Writing – review & editing, Visualization, Supervision, Methodology, Conceptualization. **Fabian Senf:**

Writing – review & editing, Visualization, Validation, Methodology.

Declaration of competing interest

The authors declare that they have no known competing financial interests or personal relationships that could have appeared to influence the work reported in this paper.

Acknowledgments

This work was supported by the Third Pole Environment program through a grant from the Chinese Academy of Sciences (XDA20060400). Finalisation of this work was supported by the Deutsche Forschungsgemeinschaft (DFG, German Research Foundation) – project number 513446258. The simulations were enabled by the computing resources provided by the National Academic Infrastructure for Supercomputing in Sweden (NAISS), partially funded by the Swedish Research Council through grant agreement no. 2022-06725. It is a contribution to the Swedish national strategic research program MERGE and CORDEX-FPS-CPTP. We are also grateful to Prof. Deliang Chen for the insightful discussions that enhanced this research. Lastly, we acknowledge the use of the WRF-Python and MetPy Python tools for data analysis.

Appendix A. Supplementary data

Supplementary data to this article can be found online at <https://doi.org/10.1016/j.atmosres.2025.108366>.

Data availability

The ERA5 data were obtained from the Copernicus Climate Change Service Information (<https://www.ecmwf.int/en/forecasts/datasets/reanalysis-datasets/era5>, accessed 15 September 2023). The GPM-IMERG and GLDAS products were provided by NASA (<https://gpm.nasa.gov/data/imerg> and <https://ldas.gsfc.nasa.gov/gldas>, accessed 22 September 2023 and 20 October 2023). The APHRODITE data can be accessed via the APHRODITE project's official website (<https://www.chikyu.ac.jp/precip/english/>, accessed 7 October 2023). MSWEP is available at the NCEP National Center for Atmospheric research website (<https://climatedataguide.ucar.edu/climate-data/global-high-resolution-precipitation-mswep>, accessed 19 October 2024).

References

- Ayantobo, O.O., Wei, J., Hou, M., Xu, J., Wang, G., 2022. Characterizing potential sources and transport pathways of intense moisture during extreme precipitation events over the Tibetan Plateau. *J. Hydrol.* 615, 128734. <https://doi.org/10.1016/j.jhydrol.2022.128734>.
- Bae, S.Y., Hong, S.-Y., Tao, W.-K., 2019. Development of a Single-Moment Cloud Microphysics Scheme with Prognostic Hail for the Weather Research and forecasting (WRF) Model. *Asia-Pac. J. Atmos. Sci.* 55 (2), 233–245. <https://doi.org/10.1007/s13143-018-0066-3>.
- Bao, Z., Zhang, J., Lian, Y., Wang, G., Jin, J., Ning, Z., Zhang, J., Liu, Y., Wang, X., 2024. Changes in Headwater Streamflow from Impacts of climate Change in the Tibetan Plateau. *Engineering* 34, 133–142. <https://doi.org/10.1016/j.eng.2023.05.025>.
- Beck, H.E., Van Dijk, A.I.J.M., Levizzani, V., Schellekens, J., Miralles, D.G., Martens, B., De Roo, A., 2017a. MSWEP: 3-hourly 0.25° global gridded precipitation (1979–2015) by merging gauge, satellite, and reanalysis data. *Hydrol. Earth Syst. Sci.* 21 (1), 589–615. <https://doi.org/10.5194/hess-21-589-2017>.
- Beck, H.E., Vergopolan, N., Pan, M., Levizzani, V., Van Dijk, A.I.J.M., Weedon, G.P., Brocca, L., Pappenberger, F., Huffman, G.J., Wood, E.F., 2017b. Global-scale evaluation of 22 precipitation datasets using gauge observations and hydrological modeling. *Hydrol. Earth Syst. Sci.* 21 (12), 6201–6217. <https://doi.org/10.5194/hess-21-6201-2017>.
- Beck, H.E., Wood, E.F., Pan, M., Fisher, C.K., Miralles, D.G., Van Dijk, A.I.J.M., McVicar, T.R., Adler, R.F., 2019. MSWEP V2 Global 3-Hourly 0.1° Precipitation: Methodology and Quantitative Assessment. *Bull. Am. Meteorol. Soc.* 100 (3), 473–500. <https://doi.org/10.1175/BAMS-D-17-0138.1>.
- Bryan, G.H., Morrison, H., 2012. Sensitivity of a simulated Squall Line to Horizontal Resolution and Parameterization of Microphysics. *Mon. Weather Rev.* 140 (1), 202–225. <https://doi.org/10.1175/MWR-D-11-00046.1>.
- Chen, Y., Wang, H., Min, J., Huang, X.-Y., Minnis, P., Zhang, R., Haggerty, J., Palikonda, R., 2015. Variational Assimilation of Cloud Liquid/Ice Water Path and its Impact on NWP. *J. Appl. Meteorol. Climatol.* 54 (8), 1809–1825. <https://doi.org/10.1175/JAMC-D-14-0243.1>.
- Chen, Y., Zhang, R., Meng, D., Min, J., Zhang, L., 2016. Variational assimilation of satellite cloud water/ice path and microphysics scheme sensitivity to the assimilation of a rainfall case. *Adv. Atmos. Sci.* 33 (10), 1158–1170. <https://doi.org/10.1007/s00376-016-6004-3>.
- Chen, A., Chen, D., Azorin-Molina, C., 2018. Assessing reliability of precipitation data over the Mekong River Basin: a comparison of ground-based, satellite, and reanalysis datasets. *Int. J. Climatol.* 38 (11), 4314–4334. <https://doi.org/10.1002/joc.5670>.
- Curio, J., Schiemann, R., Hodges, K.I., Turner, A.G., 2019. Climatology of Tibetan Plateau Vortices in Reanalysis Data and a High-Resolution Global Climate Model. *J. Clim.* 32 (6), 1933–1950. <https://doi.org/10.1175/JCLI-D-18-0021.1>.
- Dai, A., 2024. The diurnal cycle from observations and ERA5 in precipitation, clouds, boundary layer height, buoyancy, and surface fluxes. *Clim. Dyn.* <https://doi.org/10.1007/s00382-024-07182-6>.
- Dai, Y., Chen, D., Yao, T., Wang, L., 2020. Large lakes over the Tibetan Plateau may boost snow downwind: implications for snow disaster. *Sci. Bull.* 65 (20), 1713–1717. <https://doi.org/10.1016/j.scib.2020.06.012>.
- De Meij, A., Vinuesa, J.-F., Maupas, V., 2018. GHI calculation sensitivity on microphysics, land- and cumulus parameterization in WRF over the Reunion Island. *Atmos. Res.* 204, 12–20. <https://doi.org/10.1016/j.atmosres.2018.01.008>.
- Deng, Y., Wang, X., Ruan, H., Lin, J., Chen, X., Chen, Y., Duan, W., Deng, H., 2024. The magnitude and frequency of detected precipitation determine the accuracy performance of precipitation data sets in the high mountains of Asia. *Sci. Rep.* 14 (1), 17251. <https://doi.org/10.1038/s41598-024-67665-8>.
- Ding, Y., Wang, F., Lu, Z., Sun, P., Wei, R., Zhou, L., Ao, T., 2024. Assessments of various precipitation product performances and disaster monitoring utilities over the Tibetan Plateau. *Sci. Rep.* 14 (1), 19740. <https://doi.org/10.1038/s41598-024-70547-8>.
- Douville, H., Raghavan, K., Renwick, J., Allan, R.P., Arias, P.A., Barlow, M., Cerezo, Mota, R., Cherchi, A., Gan, T.Y., Gergis, J., et al., 2021. Water cycle changes. In: *Climate Change 2021: The Physical Science Basis. Contribution of Working Group I to the Sixth Assessment Report of the Intergovernmental Panel on Climate Change*.
- Eaton, B., 2011. User's Guide to the Community Atmosphere Model CAM-5.1. NCAR. <http://www.cesm.ucar.edu/models/cesm1.0/cam>.
- Feng, X., Liu, C., Rasmussen, R., Fan, G., 2014. A 10-yr Climatology of Tibetan Plateau Vortices with NCEP Climate Forecast System Reanalysis. *J. Appl. Meteorol. Climatol.* 53 (1), 34–46. <https://doi.org/10.1175/JAMC-D-13-014.1>.
- Feng, Z., Leung, L.R., Houze, R.A., Hagos, S., Hardin, J., Yang, Q., Han, B., Fan, J., 2018. Structure and Evolution of Mesoscale Convective Systems: Sensitivity to Cloud Microphysics in Convection-Allowing Simulations over the United States. *J. Adv. Model. Earth Syst.* 10 (7), 1470–1494. <https://doi.org/10.1029/2018MS001305>.
- Gao, W., Liu, L., Li, J., Lu, C., 2018. The Microphysical Properties of Convective Precipitation over the Tibetan Plateau by a Subkilometer Resolution Cloud-Resolving simulation. *J. Geophys. Res. Atmos.* 123 (6), 3212–3227. <https://doi.org/10.1002/2017JD027812>.
- Hazra, V., Pattnaik, S., Sisodiya, A., Baisya, H., Turner, A.G., Bhat, G.S., 2020. Assessing the performance of cloud microphysical parameterization over the Indian region: simulation of monsoon depressions and validation with INCOMPASS observations. *Atmos. Res.* 239, 104925. <https://doi.org/10.1016/j.atmosres.2020.104925>.
- Hersbach, H., Bell, B., Berrisford, P., Hirahara, S., Horányi, A., Muñoz-Sabater, J., Nicolas, J., Peubey, C., Radu, R., Schepers, D., Simmons, A., Soci, C., Abdalla, S., Abellán, X., Balsamo, G., Bechtold, P., Biavati, G., Bidlot, J., Bonavita, M., Thépaut, J., 2020. The ERA5 global reanalysis. *Q. J. R. Meteorol. Soc.* 146 (730), 1999–2049. <https://doi.org/10.1002/qj.3803>.
- Hou, T., Lei, H., Hu, Z., Yang, J., Li, X., 2020. Simulations of Microphysics and Precipitation in a Stratiform Cloud Case over Northern China: Comparison of two Microphysics Schemes. *Adv. Atmos. Sci.* 37 (1), 117–129. <https://doi.org/10.1007/s00376-019-8257-0>.
- Hu, X., Yuan, W., 2021. Evaluation of ERA5 precipitation over the eastern periphery of the Tibetan plateau from the perspective of regional rainfall events. *Int. J. Climatol.* 41 (4), 2625–2637. <https://doi.org/10.1002/joc.6980>.
- Huffman, G.J., Bolvin, D.T., Braithwaite, D., Hsu, K., Joyce, R., Kidd, C., Nelkin, E.J., Sorooshian, S., Tan, J., Xie, P., 2020. Nasa global precipitation measurement (gpm) integrated multi-satellite retrievals for gpm (imerg). In: *Algorithm Theoretical Basis Document Version 06*. https://gpm.nasa.gov/sites/default/files/2020-05/IMERG_ATBD_V06.3.pdf.
- Immerzeel, W.W., Lutz, A.F., Andrade, M., Bahl, A., Biemans, H., Bolch, T., Hyde, S., Brumby, S., Davies, B.J., Elmore, A.C., Emmer, A., Feng, M., Fernández, A., Haritashya, U., Kargel, J.S., Koppes, M., Kraaijenbrink, P.D.A., Kulkarni, A.V., Mayewski, P.A., Baillie, J.E.M., 2020. Importance and vulnerability of the world's water towers. *Nature* 577 (7790), 364–369. <https://doi.org/10.1038/s41586-019-1822-y>.
- Jiang, H., Yi, Y., Xu, J., Chen, D., Lu, F., Li, R., Wang, X., Zhou, B., 2023. Characterizing precipitation uncertainties in a high-altitudinal permafrost watershed of the Tibetan plateau based on regional water balance and hydrological model simulations. *J. Hydrol. Reg. Stud.* 47, 101445. <https://doi.org/10.1016/j.ejrh.2023.101445>.
- Karki, R., Hasson, S.U., Schickhoff, U., Scholten, T., Böhner, J., 2017. Rising precipitation extremes across Nepal. *Climate* 5 (1), 4. <https://doi.org/10.3390/cli5010004>.
- Karki, R., Hasson, S.U., Gerlitz, L., Talchhabadel, R., Schenk, E., Schickhoff, U., Scholten, T., Böhner, J., 2018. WRF-based simulation of an extreme precipitation event over the Central Himalayas: Atmospheric mechanisms and their representation by microphysics parameterization schemes. *Atmos. Res.* 214, 21–35. <https://doi.org/10.1016/j.atmosres.2018.07.016>.

- Kukulies, J., Chen, D., Curio, J., 2021. The role of mesoscale convective systems in precipitation in the Tibetan Plateau Region. *J. Geophys. Res. Atmos.* 126 (23), e2021JD035279. <https://doi.org/10.1029/2021JD035279>.
- Kukulies, J., Lai, H.-W., Curio, J., Feng, Z., Lin, C., Li, P., Ou, T., Sugimoto, S., Chen, D., 2023a. Mesoscale convective systems in the third pole region: Characteristics, mechanisms and impact on precipitation. *Front. Earth Sci.* 11, 1143380. <https://doi.org/10.3389/feart.2023.1143380>.
- Kukulies, J., Prein, A.F., Curio, J., Yu, H., Chen, D., 2023b. Kilometer-Scale multimodel and multiphysics ensemble simulations of a mesoscale convective system in the Lee of the Tibetan Plateau: implications for climate simulations. *J. Clim.* 36 (17), 5963–5987. <https://doi.org/10.1175/JCLI-D-22-0240.1>.
- Kumar, M., Hodnebrog, Ø., Sophie Daloz, A., Sen, S., Badiger, S., Krishnaswamy, J., 2021. Measuring precipitation in Eastern Himalaya: ground validation of eleven satellite, model and gauge interpolated gridded products. *J. Hydrol.* 599, 126252. <https://doi.org/10.1016/j.jhydrol.2021.126252>.
- Lai, H., Chen, D., Chen, H.W., 2024. Precipitation variability related to atmospheric circulation patterns over the Tibetan Plateau. *Int. J. Climatol.* 44 (1), 91–107. <https://doi.org/10.1002/joc.8317>.
- Lim, K.-S.S., Hong, S.-Y., 2010. Development of an Effective Double-Moment Cloud Microphysics Scheme with Prognostic Cloud Condensation Nuclei (CCN) for Weather and Climate Models. *Mon. Weather Rev.* 138 (5), 1587–1612. <https://doi.org/10.1175/2009MWR2968.1>.
- Lin, Y., Colle, B.A., 2011. A New Bulk Microphysical Scheme that includes riming intensity and temperature-dependent ice characteristics. *Mon. Weather Rev.* 139 (3), 1013–1035. <https://doi.org/10.1175/2010MWR3293.1>.
- Lin, C., Chen, D., Yang, K., Ou, T., 2018. Impact of model resolution on simulating the water vapor transport through the Central Himalayas: Implication for models' wet bias over the Tibetan Plateau. *Clim. Dyn.* 51 (9–10), 3195–3207. <https://doi.org/10.1007/s00382-018-4074-x>.
- Lin, Z., Yao, X., Guo, W., Du, J., Zhou, Z., 2022. Extreme precipitation events over the Tibetan Plateau and its vicinity associated with Tibetan Plateau vortices. *Atmos. Res.* 280, 106433. <https://doi.org/10.1016/j.atmosres.2022.106433>.
- Lin, Q., Chen, J., Ou, T., Lai, H., Prein, A.F., Chen, D., 2023. Performance of the WRF Model at the Convective-Permitting Scale in Simulating Snowfall and Lake-effect Snow over the Tibetan Plateau. *J. Geophys. Res. Atmos.* 128 (16), e2022JD038433. <https://doi.org/10.1029/2022JD038433>.
- Liú, J., Yang, K., Wang, J., Zhou, X., Jiang, Y., Shao, C., Lu, H., Yao, X., Sun, J., Shi, J., 2024. Impacts of a shallow convection scheme on kilometer-scale atmospheric simulations over the Tibetan Plateau. *Clim. Dyn.* 62 (8), 8019–8034. <https://doi.org/10.1007/s00382-024-07320-0>.
- Lin, Y., Liu, L., Cheng, L., Li, X., Li, H., Xu, Z., 2021. Assessment of GCMs simulation performance for precipitation and temperature from CMIP5 to CMIP6 over the Tibetan Plateau. *Int. J. Climatol.* 41 (7), 3994–4018. <https://doi.org/10.1002/joc.7055>.
- Lv, M., Xu, Z., Yang, Z., 2020. Cloud resolving WRF simulations of precipitation and soil moisture over the Central Tibetan Plateau: an assessment of various physics options. *Earth Space Sci.* 7 (2), e2019EA000865. <https://doi.org/10.1029/2019EA000865>.
- Lyu, Y., Yong, B., Huang, F., Qi, W., Tian, F., Wang, G., Zhang, J., 2024. Investigating two mainstream global precipitation datasets: which one performs better on the Tibetan Plateau? *J. Hydrol.* 633, 130947. <https://doi.org/10.1016/j.jhydrol.2024.130947>.
- Martínez-Castro, D., Kumar, S., Flores Rojas, J.L., Moya-Álvarez, A., Valdivia-Prado, J. M., Villalobos-Puma, E., Castillo-Velarde, C.D., Silva-Vidal, Y., 2019. The impact of microphysics parameterization in the simulation of two convective rainfall events over the Central Andes of Peru using WRF-ARW. *Atmosphere* 10 (8), 442. <https://doi.org/10.3390/atmos10080442>.
- Maussion, F., Scherer, D., Mölg, T., Collier, E., Curio, J., Finkelnburg, R., 2014. Precipitation seasonality and variability over the Tibetan Plateau as resolved by the high Asia reanalysis*. *J. Clim.* 27 (5), 1910–1927. <https://doi.org/10.1175/JCLI-D-13-00282.1>.
- Morrison, H., Thompson, G., Tatarki, V., 2009. Impact of cloud microphysics on the development of trailing stratiform precipitation in a simulated squall line: comparison of One- and Two-moment schemes. *Mon. Weather Rev.* 137 (3), 991–1007. <https://doi.org/10.1175/2008MWR2556.1>.
- Orr, A., Listowski, C., Couttet, M., Collier, E., Immerzeel, W., Deb, P., Bannister, D., 2017. Sensitivity of simulated summer monsoonal precipitation in Langtang Valley, Himalaya, to cloud microphysics schemes in WRF. *J. Geophys. Res. Atmos.* 122 (12), 6298–6318. <https://doi.org/10.1002/2016JD025801>.
- Ouyang, L., Lu, H., Yang, K., Leung, L.R., Wang, Y., Zhao, L., Zhou, X., Lazhu Chen, Y., Jiang, Y., Yao, X., 2021. Characterizing uncertainties in ground "Truth" of precipitation over complex terrain through high-resolution numerical modeling. *Geophys. Res. Lett.* 48 (10), e2020GL091950. <https://doi.org/10.1029/2020GL091950>.
- Pan, X., Wu, H., Chen, S., Nanding, N., Huang, Z., Chen, W., Li, C., Li, X., 2023. Evaluation and applicability analysis of GPM Satellite precipitation over mainland China. *Remote Sens.* 15 (11), 2866. <https://doi.org/10.3390/rs15112866>.
- Podet, S.R., Ramakrishna, S.S.V.S., Viswanadhapalli, Y., Dasari, H., Nellipudi, N.R., Rao, B.R.S., 2020. Sensitivity of Cloud Microphysics on the simulation of a Monsoon Depression over the Bay of Bengal. *Pure Appl. Geophys.* 177 (11), 5487–5505. <https://doi.org/10.1007/s0024-020-02557-2>.
- Pörtner, H.-O., Roberts, D.C., Masson-Delmotte, V., Zhai, P., Tignor, M., Poloczanska, E., Weyér, N., 2019. The Ocean and Cryosphere in a Changing Climate. *IPCC Special Report on the Ocean and Cryosphere in a Changing Climate*.
- Powers, J.G., Klemm, J.B., Skamarock, W.C., Davis, C.A., Dudhia, J., Gill, D.O., Coen, J.L., Gochis, D.J., Ahmadov, R., Peckham, S.E., Grell, G.A., Michalakes, J., Trahan, S., Benjamin, S.G., Alexander, C.R., Dimego, G.J., Wang, W., Schwartz, C.S., Romine, G., S., Duda, M.G., 2017. The Weather Research and forecasting Model: Overview, System efforts, and Future Directions. *Bull. Am. Meteorol. Soc.* 98 (8), 1717–1737. <https://doi.org/10.1175/BAMS-D-15-00308.1>.
- Prein, A.F., Ban, N., Ou, T., Tang, J., Sakaguchi, K., Collier, E., Jayanarayanan, S., Li, L., Sobolowski, S., Chen, X., Zhou, X., Lai, H.-W., Sugimoto, S., Zou, L., Hasson, S., Ul Ekstrom, M., Pothapakula, P.K., Ahrens, B., Stuart, R., Chen, D., 2023. Towards Ensemble-based Kilometer-Scale climate Simulations over the Third Pole Region. *Clim. Dyn.* 60 (11–12), 4055–4081. <https://doi.org/10.1007/s00382-022-06543-3>.
- Reshma Mohan, P., Srinivas, C.V., Yesubabu, V., Baskaran, R., Venkatraman, B., 2018. Simulation of a heavy rainfall event over Chennai in Southeast India using WRF: Sensitivity to microphysics parameterization. *Atmos. Res.* 210, 83–99. <https://doi.org/10.1016/j.atmosres.2018.04.005>.
- Roberts, N.M., Lean, H.W., 2008. Scale-selective verification of rainfall accumulations from high-resolution forecasts of convective events. *Mon. Weather Rev.* 136 (1), 78–97. <https://doi.org/10.1175/2007MWR2123.1>.
- Rodell, M., Houser, P.R., Jambor, U., Gottschalck, J., Mitchell, K., Meng, C.-J., Arsenault, K., Cosgrove, B., Radakovitch, J., Bosilovich, M., Entin, J.K., Walker, J.P., Lohmann, D., Toll, D., 2004. The Global Land Data Assimilation System. *Bull. Am. Meteorol. Soc.* 85 (3), 381–394. <https://doi.org/10.1175/BAMS-85-3-381>.
- Segele, Z.T., Leslie, L.M., Lamb, P.J., 2013. Weather Research and forecasting Model simulations of extended warm-season heavy precipitation episode over the US Southern Great Plains: Data assimilation and microphysics sensitivity experiments. *Tellus A Dyn. Meteorol. Oceanogr.* 65 (1), 19599. <https://doi.org/10.3402/tellusa.v65i0.19599>.
- Shao, X., Zhang, Y., Ma, N., Zhang, X., Tian, J., Liu, C., 2023. Flood increase and Drought Mitigation under a Warming climate in the Southern Tibetan Plateau. *J. Geophys. Res. Atmos.* 128 (2), e2022JD037835. <https://doi.org/10.1029/2022JD037835>.
- Shen, S., Xiao, H., Yang, H., Fu, D., Shu, W., 2021. Variations of water vapor transport and water vapor-hydrometeor-precipitation conversions during a heavy rainfall event in the Three-River-Headwater region of the Tibetan Plateau. *Atmos. Res.* 264, 105874. <https://doi.org/10.1016/j.atmosres.2021.105874>.
- Shukla, A., Pattnaik, S., Trivedi, D., 2022. Study of Mesoscale Convective System and its Associated Cloud Structure over Indian Region using Satellite Observations and Model Simulations. *J. Indian Soc. Remote Sens.* 50 (10), 1885–1901. <https://doi.org/10.1007/s12524-022-01573-0>.
- Skamarock, W.C., Klemp, J.B., Dudhia, J., Gill, D.O., Liu, Z., Berner, J., Wang, W., Powers, J.G., Duda, M.G., Barker, D.M., Huang, X.-Y., 2019. A Description of the Advanced Research WRF Model Version 4. UCAR/NCAR. <https://doi.org/10.5065/1DFH-6P97>.
- Sohn, S., Tam, C., Ashok, K., Ahn, J., 2012. Quantifying the reliability of precipitation datasets for monitoring large-scale East Asian precipitation variations. *Int. J. Climatol.* 32 (10), 1520–1526. <https://doi.org/10.1002/joc.2380>.
- Tan, X., Ma, Z., He, K., Han, X., Ji, Q., He, Y., 2020. Evaluations on gridded precipitation products spanning more than half a century over the Tibetan Plateau and its surroundings. *J. Hydrol.* 582, 124455. <https://doi.org/10.1016/j.jhydrol.2019.124455>.
- Tan, M.L., Goliat, L., Heddam, S., Abdul Maulud, K.N., Halder, B., Sa'adi, Z., Ahmadianfar, I., Shafiq, S.S., Ali, M., Yaseen, Z.M., 2025. A Review of APHRODITE Performance in Asia: current status and research concerns. *J. Hydrol.* 651, 132562. <https://doi.org/10.1016/j.jhydrol.2024.132562>.
- Tang, J., Guo, X., Chang, Y., 2019. A Numerical Investigation on Microphysical Properties of Clouds and Precipitation over the Tibetan Plateau in Summer 2014. *J. Meteorol. Res.* 33 (3), 463–477. <https://doi.org/10.1007/s13351-019-8614-z>.
- Thomas, B., Viswanadhapalli, Y., Srinivas, C.V., Dasari, H.P., Attada, R., Langodan, S., 2021. Cloud resolving simulation of extremely heavy rainfall event over Kerala in August 2018 – Sensitivity to microphysics and aerosol feedback. *Atmos. Res.* 258, 105613. <https://doi.org/10.1016/j.atmosres.2021.105613>.
- Thompson, G., Field, P.R., Rasmussen, R.M., Hall, W.D., 2008. Explicit forecasts of Winter Precipitation using an improved Bulk Microphysics Scheme. Part II: Implementation of a New Snow Parameterization. *Mon. Weather Rev.* 136 (12), 5095–5115. <https://doi.org/10.1175/2008MWR2387.1>.
- Tiwari, S., Kar, S.C., Bhatia, R., 2018. Dynamic downscaling over western Himalayas: Impact of cloud microphysics schemes. *Atmos. Res.* 201, 1–16. <https://doi.org/10.1016/j.atmosres.2017.10.007>.
- Van Weverberg, K., Vogelmann, A.M., Lin, W., Luke, E.P., Cialella, A., Minnis, P., Khaiyer, M., Boer, E.R., Jensen, M.P., 2013. The Role of Cloud Microphysics Parameterization in the simulation of Mesoscale Convective System Clouds and Precipitation in the Tropical Western Pacific. *J. Atmos. Sci.* 70 (4), 1104–1128. <https://doi.org/10.1175/JAS-D-12-0104.1>.
- Wang, W., Lin, H., Chen, N., Chen, Z., 2021. Evaluation of multi-source precipitation products over the Yangtze River Basin. *Atmos. Res.* 249, 105287. <https://doi.org/10.1016/j.atmosres.2020.105287>.
- Wu, X., Su, J., Ren, W., Lü, H., Yuan, F., 2023. Statistical comparison and hydrological utility evaluation of ERA5-Land and IMERG precipitation products on the Tibetan Plateau. *J. Hydrol.* 620, 129384. <https://doi.org/10.1016/j.jhydrol.2023.129384>.
- Xu, Z.X., Gong, T.L., Li, J.Y., 2008. Decadal trend of climate in the Tibetan Plateau—Regional temperature and precipitation. *Hydrol. Process.* 22 (16), 3056–3065. <https://doi.org/10.1002/hyp.6892>.
- Xu, J., Ma, Z., Yan, S., Peng, J., 2022. Do ERA5 and ERA5-land precipitation estimates outperform satellite-based precipitation products? A comprehensive comparison between state-of-the-art model-based and satellite-based precipitation products over mainland China. *J. Hydrol.* 605, 127353. <https://doi.org/10.1016/j.jhydrol.2021.127353>.
- Yang, Q., Yu, Z., Wei, J., Yang, C., Gu, H., Xiao, M., Shang, S., Dong, N., Gao, L., Arnault, J., Laux, P., Kunstmänn, H., 2021. Performance of the WRF model in simulating intense precipitation events over the Hanjiang River Basin, China – a

- multi-physics ensemble approach. *Atmos. Res.* 248, 105206. <https://doi.org/10.1016/j.atmosres.2020.105206>.
- Yatagai, A., Kamiguchi, K., Arakawa, O., Hamada, A., Yasutomi, N., Kitoh, A., 2012. APHRODITE: Constructing a Long-Term Daily Gridded Precipitation Dataset for Asia based on a Dense Network of rain Gauges. *Bull. Am. Meteorol. Soc.* 93 (9), 1401–1415. <https://doi.org/10.1175/BAMS-D-11-00122.1>.
- Yuan, X., Yang, K., Lu, H., He, J., Sun, J., Wang, Y., 2021. Characterizing the features of precipitation for the Tibetan Plateau among four gridded datasets: detection accuracy and spatio-temporal variabilities. *Atmos. Res.* 264, 105875. <https://doi.org/10.1016/j.atmosres.2021.105875>.
- Zhang, T., Schultz, D.M., 2024. Cold-Frontal Rainbands over the United Kingdom: Sensitivity of Precipitation Processes to Microphysics Schemes in WRF Simulations. *Mon. Weather Rev.* 152 (11), 2393–2418. <https://doi.org/10.1175/MWR-D-24-0011.1>.
- Zhang, Y., Ouyang, X., Wang, M., Rosenfeld, D., Zhao, D., Wu, X., 2024. Evaluating Ice phase Microphysics in the simulation of a Snowstorm over Northern China. *J. Geophys. Res. Atmos.* 129 (6), e2023JD040221. <https://doi.org/10.1029/2023JD040221>.
- Zhou, Y., Liu, L., Deng, G., 2009. Comparisons of the Generalized potential Temperature in Moist Atmosphere with the Equivalent potential Temperature in Saturated Moist Atmosphere. *Adv. Meteorol.* 2009, 1–9. <https://doi.org/10.1155/2009/105265>.
- Zhou, P., Ma, M., Shao, M., Tang, J., 2024. Sensitivity of summer precipitation simulation to the physical parameterizations in WRF over the Tibetan Plateau: a case study of 2018. *Atmos. Res.* 299, 107174. <https://doi.org/10.1016/j.atmosres.2023.107174>.